Seismic site characterization using broadband and DAS ambient vibration measurements on Mt Etna, Italy

Master thesis

Helmholtz Centre Potsdam
GFZ German Research Centre for Geosciences
Section 2.2 - Geophysical Imaging

Institute of Geosciences
Faculty of Sciences
University of Potsdam

submitted by: **Jonas Pätzel (783143)**

supervised by: Dr. Philippe Jousset (GFZ Potsdam)
Dr. Matthias Ohrnberger (University of Potsdam)

May 26, 2023

Abstract

Both horizontal-to-vertical (H/V) spectral ratios and the spatial autocorrelation method (SPAC) have proven to be valuable tools to gain insight into local site effects by ambient noise measurements. Here, the two methods are employed to assess the subsurface velocity structure at the Piano delle Concazze area on Mt Etna.

Volcanic tremor records from an array of 26 broadband seismometers is processed and a strong variability of H/V ratios during periods of increased volcanic activity is found. From the spatial distribution of H/V peak frequencies, a geologic structure in the northeast of Piano delle Concazze is imaged which is interpreted as the Ellittico caldera rim. The method is extended to include both velocity data from the broadband stations and distributed acoustic sensing data from a co-located 1.5 km long fibre optic cable. High maximum amplitude values of the resulting ratios along the trajectory of the cable coincide with known faults. The outcome also indicates previously unmapped parts of a fault. The geologic interpretation is in good agreement with inversion results from magnetic survey data.

Using the neighborhood algorithm, spatial autocorrelation curves obtained from the modified SPAC are inverted alone and jointly with the H/V peak frequencies for 1D shear wave velocity profiles. The obtained models are largely consistent with published models and were able to validate the results from the fibre optic cable.

Kurzzusammenfassung

Sowohl die räumliche Autokorrelations-Methode (SPAC) als auch die Methode der horizontal-vertikal Spektralverhältnisse (H/V) sind wichtige Instrumente bei der seismischen Charakterisierung des Untergrundes mittels Bodenunruhe.

In der vorliegenden Arbeit werden beide Techniken angewandt, um die Geschwindigkeitsstruktur der Piano delle Concazze Ebene auf dem Ätna zu untersuchen. Die Aufzeichnungen vulkanischen Tremors auf einem Array aus 26 Breitband-Seismometern werden prozessiert und starke Schwankungen des H/V Verhältnisses, insbesondere während Zeiten erhöhter vulkanischer Aktivität werden festgestellt. Die räumliche Verteilung der H/V Frequenzpeaks bildet eine geologische Struktur im nordöstlichen Bereichs des Untersuchungsgebietes ab. Diese wird als der alte Rand der Ellittico Caldera interpretiert. Die H/V-Methode wird um die kombinierte Verarbeitung von Geschwindigkeitsaufzeichnungen des Breitband-Arrays und faseroptischen Dehnungmessungen (*distributed acoustic sensing*, DAS) erweitert. Hierfür werden die Daten eines 1,5 km langen Glasfaserkabels, mit welchem das Seismometer-Array zusammen installiert wurde, genutzt. Erhöhte Werte der maximalen Amplitude der berechneten Spektralverhältnisse, stimmen mit der Lage bekannter Verwerfungen im Gebiet überein. Das Ergebnis deutet auf einen bisher nicht aufgezeichneten Verlauf einer der Verwerfungszonen hin. Die Interpretaion der Strukturen stimmt überein mit den Ergebnissen einer Geomagnetik-Studie der Piano delle Concazze.

Mithilfe des Neighborhood-Algorithmus werden die räumlichen Autokorrelationskurven der modifizierten SPAC, sowohl einfach als auch in Kombination mit den H/V Frequenzpeaks, invertiert. So werden schließlich 1D Modelle der S-Wellengeschwindigkeit abgeleitet. Diese stimmen weitgehend überein mit den Resultaten anderer Studien und bestätigen darüberhinaus die Ergebnisse der DAS-Aufzeichnungen.

List of abbreviations and symbols

Abbreviations

a.s.l.	above sea level
BAZ	backazimuth
DAS	distributed acoustic sensing
DC	dispersion curve
FAS	Fourier amplitude spectrum
f-k analysis	frequency-wavenumber analysis
HVSR, H/V	horizontal-to-vertical spectral ratio
INGV	Instituto Nazionale di Geofisica e Vulcanologia
LP	long-period
MSPAC	modified spatial autocorrelation method
NA	neighbourhood algorithm
PDC	Piano delle Concazze
RMS	root mean square
SPAC	spatial autocorrelation (method)
STA/LTA	short time average/long time average

Symbols

A_0	amplitude of HVSR curve at f_0 [-]
$A_{H/V}(f)$	amplitude of HVSR curve at f [-]
c	phase velocity $[\frac{m}{s}]$
d	layer bottom depth [m]
f	frequency [Hz]
f_0	fundamental frequency, H/V peak frequency [Hz]
h	layer thickness [m]
J_n	Bessel function of first kind and n-th order
l_w	time window length [s]
n_w	number of time windows
P	power spectral density $[\frac{(\frac{m}{s})^2}{Hz}]$
r	distance/radius [m]
v_P	P-wave velocity $[\frac{m}{s}]$
v_S	S-wave velocity $[\frac{m}{s}]$
$\overline{x}$	azimuthal averaging of x
$< x >$	temporal averaging of x
$\|x\|$	absolute value of x
δ	Dirac delta function
λ	wavelength [m]
ν	Poisson's ratio [-]
ρ	auto correlation coefficient [-]
ϱ	density $[\frac{kg}{m^3}]$
σ_f	standard deviation of f_0 [Hz]
$\sigma_A(f)$	standard deviation of $A_{H/V}$ at f [-]
ϕ	spatial correlation function

Φ	power spectrum $[(\frac{m}{s})^2]$
φ	azimuth [rad]
ω	angular frequency [Hz]

Contents

Appendices

1. Introduction

Volcano seismology is a fundamental tool to further our understanding of volcanoes and their underlying principles and mechanisms.
As nearly all volcanic processes produce individual seismic signals, their records allow to assess the state of a volcanic system as well as imaging its composition (Kawakatsu & Yamamoto, 2015). Conventionally, volcano-seismic measurements are performed using three component broadband seismometers (Chouet, 2003). However, over the last years, new sensing technologies have become more popular to gain insight into the structure and behaviour of volcanoes. This includes rotational sensors and distributed acoustic sensing (DAS). While rotational sensors record not translational but the rotational components of seismic signals, the latter is able to sample the wavefield much more spatially dense than any normal seismometer array (Eibl et al., 2022; Jousset et al., 2022). However, due to the only recent widespread deployment of these new sensors for seismological research, their performance, advantages and shortcomings are still being evaluated.

This study attempts to characterize a specific site at Mt Etna, using conventional surface wave methods. By that, results that have been obtained by DAS on a fibre optic cable can be compared and may be validated. The site characterization is achieved by processing the volcanic tremor recorded on a co-located array of broadband seismometers. Over the course of the work, the main subsurface structures present at the site will be imaged and an estimate of the velocity distribution in form of 1D shear wave velocity models is derived.

Further, the extension of conventional methods to the combination of broadband and DAS records will be investigated in order to derive additional subsurface features.

In the following chapter 2 the theoretical background to volcaninc tremor and the two mainly used methods, horizontal-to-vertical spectral ratios and the modified spatial autocorrelation method, will be given. Chapters 3 and 4 adress the survey area with its geological setting and volcano-seismologic framework, followed by a description of the used datasets and the instrumental setup. Chapter 5 then presents how the theoretically presented methods were implemented. The used workflow of data processing and the setting of processing parameters are given. The obtained outcomes will first be described and then discussed in detail. Comparisons with available literature will be made and possible sources of errors are adressed. Finally the results of this work will be summarized and potential further subjects of investigation will be discussed.

2. Theory

This chapter aims at giving a short introduction to the two methods used in this thesis, horizontal-to-vertical spectral ratios and the spatial autocorrelation method. Both techniques are based on the processing of seismic ambient noise (ambient vibrations, microtremors) i.e., the sustained signal of environmental and human processes (Bonnefoy-Claudet et al., 2006).

For the investigated records in this study, the predominant noise origin is the tremor generated at Mt Etna. Volcanic tremor refers to the continuous seismic signal unique to active volcanoes (Konstantinou & Schlindwein, 2003, and references therein). It is commonly described as carrying energy in a narrow frequency band between 1 Hz and 5 to 7 Hz, in some cases strong periodic peaks in the frequency spectrum can be observed. Its exact excitation mechanism and the distinction from volcanic low-frequency/long-period (LP) events is still being debated (Kawakatsu & Yamamoto, 2015; McNutt, 2005; Wassermann, 2009).

It has been noted, that volcanic tremor is a suitable noise source for the assessment of site effects on volcanoes. This is due to its stationary nature and the large proportion of surface waves in the signal, both is essential for the spatial autocorrelation method (e.g., Chouet, 1996; Konstantinou & Schlindwein, 2003).

In the following, first the H/V-method is presented, ensued by the spatial autocorrelation method and its modification. A brief overview of the fundamental principles, the applications and the essential equations will be given.

2.1. The H/V-method

Since the initial work of Nakamura (1989), the horizontal-to-vertical spectral ratio method (HVSR, H/V) has been demonstrated to be an inexpensive and easy to use technique to assess local site effects. Numerous studies are available that demonstrate the potential of H/V to infer the fundamental resonance frequency of a site in order to characterize the subsurface, often to assess seismic vulnerability of urban agglomerations (e.g., Lermo & Chávez-García, 1993). Other studies can be found presenting results from a wide range of geologic settings and surroundings, even investigating locations on Moon and Mars (e.g., Hobiger et al., 2021). As is the aim of the present work, the method has also been successfully used to retrieve subsoil information in particular on active volcanoes (e.g., Mora et al., 2001; Nardone & Maresca, 2011; Vidal-Villegas et al., 2021).
Despite the widespread use of HVSR and the efforts to provide comprehensive guidelines (Foti et al., 2017; SESAME, 2004), authors have been and are still lamenting a lack of standards for data aquisition and processing as well as theoretical understanding of the method (e.g., Bonnefoy-Claudet et al., 2006; Molnar et al., 2022; Mucciarelli & Gallipoli, 2001; Xu & Wang, 2021).

The fundamental principle of HVSR is the computation of the ratio between horizontal (H_S) and vertical (V_S) Fourier amplitude spectrum (FAS) of a single three-component seismic station at the ground surface. In case of an impedance contrast in depth, e.g., a layer of soft sediments over bedrock, the shape of the resulting HVSR curve contains information about this subsurface structure.

$$HVSR = \frac{H_S}{V_S} \tag{2.1}$$

H_S is a combination of the two horizontal spectra. Different methods to merge both spectra have been proposed e.g., arithmetic mean, geometric mean or vector summation.

It was found that when averaging the HVSR over multiple time samples, differences in the methods results vanish (Albarello & Lunedei, 2013). As used for example in Bonnefoy-Claudet et al. (2008), H_S in this study is derived as a quadratic mean, i.e.:

$$H_S = \sqrt{\frac{H_N^2 + H_E^2}{2}} \tag{2.2}$$

where H_N and H_E are the spectra of the north-south and east-west component respectively. In order to denoise the spectra, they are smoothed before further computation. Figure 2.1 shows as an example the smoothed spectra of all three components and the corresponding H/V ratio.

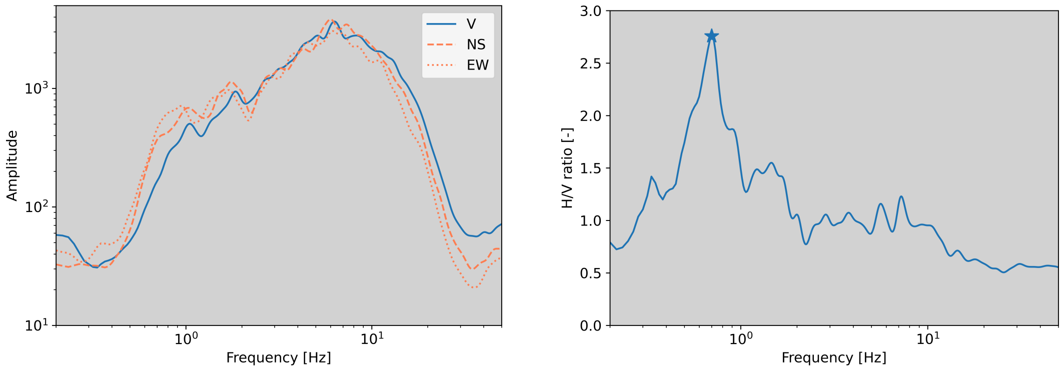

Figure 2.1.: left plot: smoothed spectra of the vertical (V), north-south (NS) and east-west (EW) component; right plot shows the resulting HVSR curve, star marks the H/V peak

As Molnar et al. (2022) notes, no single analytical expression for HVSR exists yet. This is mainly due to the still ongoing debate as to how the noise wavefield is composed. The ratio between surface waves, body waves and other diffuse waves is unclear and also strongly dependent on individual site conditions and noise sources. This uncertainty makes the modelling as well as the interpretation of HVSR curves challenging. However interpretations of different features of the H/V have already been proposed, including the computation and inversion of the full curve (e.g., Lontsi et al., 2015; Sánchez-Sesma et al., 2011).

Nevertheless, there is wide consensus that the H/V curve exhibits its first peak at the fundamental resonance frequency of the site f_0. This frequency is directly related to the thickness of the covering layer. In the general case of the n-th resonance frequency f_n, this relation is given by:

$$f_n = (2n+1)\left(\frac{v_{S,0}}{4h}\right), \quad (n = 0, 1, 2, ...) \tag{2.3}$$

where $v_{S,0}$ denotes the shear-wave velocity and h the thickness of the top layer.

This way, with an estimate of the surface shear-wave velocity obtained by other methods, the depth of the impedance contrast can be approximated easily and only using a single seismic station. Results are regarded to be very stable in time and can generally be obtained by only recording a few minutes of ambient vibrations. Further reviews of HVSR history, theory and application can be found in Molnar et al. (2018), Molnar et al. (2022), Mucciarelli and Gallipoli (2001), and Xu and Wang (2021).

In the present work HVSRs will be inverted together with spatial autocorrelation values, hence only the peak frequencies are considered as other independent information on the velocity distribution is introduced.

2.2. The spatial autocorrelation method (SPAC)

First proposed by Aki (1957), the spatial autocorrelation method (SPAC) has become a common seismological array technique to characterize the local subsurface geology. By correlating ambient seismic noise signals, it allows to derive the dispersion curves (DC) of the surface waves present in the wavefield. As the shape of DCs is dictated by the underlying propagation media, the SPAC results can then be used in an inversion process to estimate the velocity distribution of the subsurface.

Since its development, there has been a large number of studies using SPAC with different approaches, in combination with other geophysical imaging methods and in settings ranging from urban areas (e.g., Flores Estrella & González, 2002; Ikeda et al., 2013; Srigutomo et al., 2018) to active volcanic zones (e.g., Lanza et al., 2016; Maresca et al., 2006; Mora et al., 2006; Perrier et al., 2012; Saccorotti et al., 2001). Furthermore, a number of extensions, formulations and modifications of the original method have been proposed (e.g., Haney et al., 2012; Li et al., 2019; Nakahara, 2012; Nakahara et al., 2021). A more extensive review of the history and application of SPAC can be found in Ikeda et al. (2013) and, focussing on SPAC on volcanoes, in Chouet and Matoza (2013).

In the following, a brief derivation of the essential equations will be presented as well as the modification of SPAC that was applied in this study. This section follows the explanations of Chouet (1996) and Bettig et al. (2001) besides Aki (1957, 1965).
SPAC is based on a few fundamental assumptions. First, it is assumed that ambient vibrations consist mainly of surface waves; second seismic noise propagates as plane waves with a single phase velocity per frequency and third, seismic noise is assumed to be stationary in both space and time, i.e. sources are randomly distributed spatially and temporally.

Aki (1957, 1965) defines the spatial autocorrelation function $\phi(r, \varphi)$ of two signals u recorded at two stations as

$$\phi(r, \varphi) = < u(x, y, t)u(x + r\cos\varphi, y + r\sin\varphi, t) > \tag{2.4}$$

where r is the interstation distance, φ the azimuth of the connecting line between both receivers and $<>$ denotes averaging over time. Azimuthal averaging of ϕ is obtained by integrating over all φ:

$$\overline{\phi}(r) = \int_0^{\pi} \phi(r, \varphi) d\varphi \tag{2.5}$$

A Hankel transform can be used to express a given function as a weighted sum of Bessel functions. Making use of this property, the following relation between the autocorrelation function and the power spectrum $\Phi(\omega)$ is found:

$$\overline{\phi}(r) = \frac{1}{\pi} \int_0^\infty \Phi(\omega) J_0 \left(\frac{\omega r}{c(\omega)} \right) d\omega \tag{2.6}$$

with $c(\omega)$ being the frequency-dependent phase velocity and J_n denoting a n-th order Bessel function.

When the signal is filtered using a narrow bandpass filter around the center frequency ω_0, then $\Phi(\omega)$ can be expressed as

$$\Phi(\omega) = P(\omega_0)\delta(\omega - \omega_0) \tag{2.7}$$

where $P(\omega_0)$ is the power spectral density, δ is the Dirac delta function and $\omega > 0$.

Inserting 2.7 into 2.6 gives:

$$\overline{\phi}(r, \omega_0) = P(\omega_0) J_0 \left(\frac{\omega r}{c(\omega)} \right) \tag{2.8}$$

Defining the autocorrelation coefficient as

$$\rho(r, \varphi, \omega_0) = \frac{\phi(r, \varphi, \omega_0)}{\phi(0, \varphi, \omega_0)} \tag{2.9}$$

and inserting 2.8 then finally yields:

$$\overline{\rho}(r, \omega) = J_0 \left(\frac{\omega r}{c(\omega)} \right) \tag{2.10}$$

As Aki (1957) notes, this formula allows to obtain the phase velocity $c(\omega)$ from the observed $\overline{\rho}$-values.

However, 2.10 only holds for seismograms recorded on the vertical component. On the radial and transverse component of a seismogram, a superposition of two wave types can be observed: (1) waves with their horizontal component polarized parallel to the propagation direction (e.g., Rayleigh waves) and (2) waves with their horizontal component polarized normal to the propagation direction (e.g., Love waves). Expressions for $\overline{\rho_r}(r,\omega)$ and $\overline{\rho_t}(r,\omega)$ become more complex but are found following the same procedure as before:

$$\overline{\rho_r}(r,\omega) = \alpha \left[J_0\left(\frac{\omega r}{c_R(\omega)}\right) - J_2\left(\frac{\omega r}{c_R(\omega)}\right)\right] (1-\alpha) \left[J_0\left(\frac{\omega r}{c_L(\omega)}\right) + J_2\left(\frac{\omega r}{c_L(\omega)}\right)\right] \tag{2.11a}$$

$$\overline{\rho_t}(r,\omega) = \alpha \left[J_0\left(\frac{\omega r}{c_R(\omega)}\right) + J_2\left(\frac{\omega r}{c_R(\omega)}\right)\right] (1-\alpha) \left[J_0\left(\frac{\omega r}{c_L(\omega)}\right) - J_2\left(\frac{\omega r}{c_L(\omega)}\right)\right] \tag{2.11b}$$

Here $\alpha(\omega)$ and $1-\alpha(\omega)$ denote the ratio of Rayleigh and Love waves in the wave field, respectively ($0 < \alpha < 1$).

2.2.1. Modified SPAC: Extension of SPAC to imperfect array configurations

In the form presented up to this point, the SPAC works only on circular or semi-circular arrays. In order to make use of the SPAC, sensors are placed around central reference station with a constant radius and equally distributed along the azimuth. In addition to these limitations in array geometry, obtained results are only valid in a narrow frequency band which can only be expanded by repeating the experiment with varying radii. Especially for lower frequencies and corresponding large apertures, a perfectly circular array becomes impractical. Bettig et al. (2001) therefore developed the modified SPAC (MSPAC) and demonstrated the applicability of the SPAC to imperfect array configurations.

If we assume the lateral variations of the subsurface structures beneath the array to be small with respect to the array aperture, only relative locations of the sensor locations need to be considered. A pair of two stations can then be characterized by its interstation distance r and the azimuth of the connecting line between both stations φ, giving a polar coordinate. This allows us to represent all possible combinations of stations in a polar plot called the *co-array* (see figure 2.2).

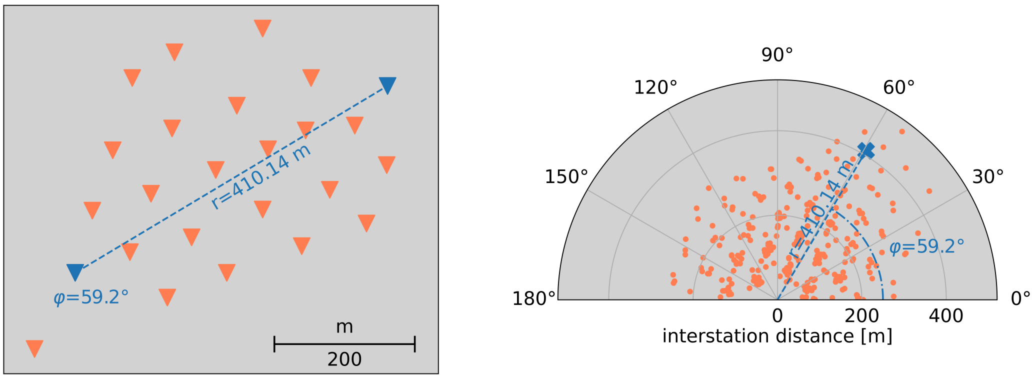

Figure 2.2.: An array configuration with the corresponding co-array on the right, one station pair and the connecting line between both stations is marked in blue in the map view, the same station pair in the co-array plot is marked with blue X

This way we can visualize all station pairs within a given range of radii by plotting a ring between the two values r_1 and r_2.

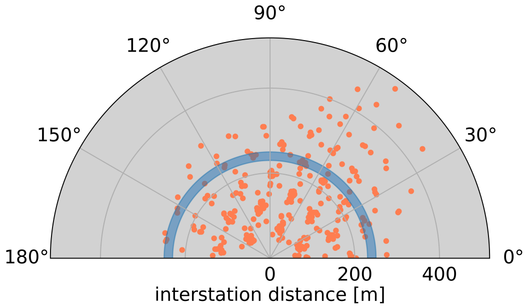

Figure 2.3.: Co-array plot with ring from $r_1 = 230$ m to $r_2 = 250$ m

The autocorrelation coefficient of station pairs within the ring can be obtained by averaging 2.10 over the range of r_1 and r_2:

$$\overline{\rho_{r_1,r_2}}(\omega) = \frac{2}{r_2^2 - r_1^1} \int_{r_1}^{r_2} r J_0 \left(\frac{\omega r}{c_R(\omega)} \right) dr \tag{2.12}$$

Using the properties of Bessel functions, this can be written as:

$$\overline{\rho_{r_1,r_2}}(\omega) = \frac{2}{r_2^2 - r_1^1} \frac{c(\omega)}{\omega} \left[r J_1 \left(\frac{\omega r}{c_R(\omega)} \right) \right]_{r_1}^{r_2} \tag{2.13}$$

The modified expressions for the horizontal components corresponding to 2.11 can be derived similarly. Köhler et al. (2007) gives:

$$\overline{\rho_{r,k}}(\omega) = \frac{4}{r_2^2 - r_1^2} \left\{ \frac{\alpha c_R}{\omega} \left(\frac{c_R}{\omega} \left[J_0\left(w_R\right) \right]_{r_1}^{r_2} + \left[r J_1\left(w_R\right) \right]_{r_1}^{r_2} \right) - \frac{(1-\alpha) c_L^2}{\omega^2} \left[J_0\left(w_L\right) \right]_{r_1}^{r_2} \right\} \tag{2.14a}$$

$$\overline{\rho_{t,k}}(\omega) = \frac{4}{r_2^2 - r_1^2} \left\{ \frac{-\alpha c_R^2}{\omega^2} \left[J_0(w_R) \right]_{r_1}^{r_2} + \frac{(1-\alpha) c_L}{\omega} \left(\frac{c_L}{\omega} \left[J_0(w_L) \right]_{r_1}^{r_2} + \left[r J_1(w_L) \right]_{r_1}^{r_2} \right) \right\} \tag{2.14b}$$

where $w_R = \frac{\omega r}{c_R(\omega)}$ and $w_L = \frac{\omega r}{c_L(\omega)}$.

We can now divide an array of seismometers into multiple sub-arrays k defined by station couples (i, j) and their respective distance r_{ij} with $r_{k1} < r_{ij} < r_{k2}$. The autocorrelation ratio for k can be computed using:

$$\overline{\rho_k}(\omega) = \frac{2}{\pi (r_{k2}^2 - r_{k1}^2)} \sum_{r_{k1} < r_{ij} < r_{k2}} \rho(r_{ij}, \varphi_{ij}, \omega) \overline{r_k} \Delta r_k \Delta \varphi_{ij} \tag{2.15}$$

with

$$\overline{r_k} = \frac{r_{k2} + r_{k1}}{2} \quad \text{and} \quad \Delta r_k = r_{k2} - r_{k1}$$

this finally becomes:

$$\overline{\rho_k}(\omega) = \frac{1}{\pi} \sum_{r_{k1} < r_{ij} < r_{k2}} \rho(r_{ij}, \varphi_{ij}, \omega) \Delta \varphi_{ij} \tag{2.16}$$

By splitting the array into smaller sub-arrays and then applying equation 2.16, two things are now achieved:

- The summation over r_{ij} accounts for varying radius values.
- A weighting mechanism is introduced that compensates for irregular distribution of station couples in azimuth. The factor $\Delta\varphi_{ij}$ is given as:

  $$\Delta\varphi_{ij} = \frac{\varphi_{ij+1} - \varphi_{ij-1}}{2} \quad \text{with} \quad \sum \Delta\varphi_{ij} = \pi$$

  This weights the autocorrelation curve of a station pair by the azimuthal distance to the neighbouring station pairs.

This method eliminates the need for a regular, circular array and therefore allows to infer SPAC results in a broader frequency range. Furthermore, the data recorded on seismological arrays originally not designed for the application of SPAC can be used for insight into the local velocity distribution and site effects.

3. Area of Interest

This chapter focuses on a short introduction of Etna's geological and geodynamic setting as well as the volcano-seismic activity present in the study area. Multidisciplinary overviews covering the detailed geological and eruptive history, statistics, research and monitoring of Etna can be found in Chester (1985), Pichler (1984) and Bonaccorso et al. (2004).

3.1. Geological and Geodynamic Setting

Mt Etna is a basaltic stratovolcano in the Central Mediterranean, located in the east of Sicily and rising to more than 3350 m at its highest point. It is considered to be the largest and most active volcano in Europe (e.g., Villaseñor et al., 1998).
Etna lies in the complex geodynamic framework of the Mediterranean, dominated by the convergence of the African tectonic plate in the south and the Eurasian plate in the north. The region of eastern Sicily with the Malta escarpment, the Calabrian arc and the Apennine chain is one of the tectonically most active areas therein, producing not only volcanism but also large earthquakes (Díaz-Moreno et al., 2017).

The recent shape of Etna is the result of an interplay of regional to continent-scale tectonics and local volcanic processes (Panzera et al., 2016). The beginning of the volcanic activity can be traced back about 500,000 years. It is followed by a succesion of eruptive phases, with the ongoing Mongibello stadium being the most recent one

(Branca et al., 2011; Díaz-Moreno et al., 2017).

Consequently, Etna is formed by a sequence of stratovolcanoes often with associated calderas. The most noticeable of which is the Ellittico caldera, approximately 15,000 years of age (Doglioni et al., 2001; Panzera et al., 2016).

The present crater area at Etna's summit encompasses four main vents: the North East Crater (NEC), the South East Crater (SEC), Bocca Nuova (BN) and Voragine (VOR). Having been formed in 1911, NEC is the oldest of the craters with VOR and BN dating back to the 1950s and 1960s respectively; The SEC has been formed most recently (1971) and is currently the most active of the craters (Chester, 1985; Pichler, 1984). Additionally, in 2011 a new cone was constructed by intense lava fountaining at the flank of the SEC. It is now referred to as the New South East Crater (NSEC; Behncke et al., 2014). More recently, NSEC and SEC have merged into one crater complex, again referred to as SEC (Bisson et al., 2021).

3.2. Seismic and Volcanic Activity

Etna exhibits a great variety of different seismic signals such as volcano-tectonic, long-period (LP) and hybrid events as well as volcanic tremor. Their variations in amplitude, frequency content, wavefield composition and waveform as well as hypocenter location are closely linked to the volcanic activity.

LP and tremor are generally interpreted as the result of interaction of fluids such as magma or gas with the volcanic edifice. They are therefore directly related to the inner dynamics of the volcano (Cannata et al., 2013; Patanè et al., 2004).

For instance, each section of the shallower part of Etna's feeding channels, generates volcanic tremor in its characteristic resonance frequency band. This allows the attribution of a tremor signal to a specific part of the feeding system. In general, any type of eruptive activity is accompanied by an increased tremor amplitude, often preceeding

the eruption itself (Pichler, 1984).
Sciotto et al. (2022) and Cannata et al. (2013) found that continuous volcanic tremor at Etna generally is recorded in the 1 to 5 Hz frequency band. Zuccarello et al. (2016) observes the 1 to 4 Hz range to be dominated by tremor. Specifically for August and September 2019, Eibl et al. (2022) notes the tremor contains energy up to 3 Hz with the spectral peak around 1 Hz.

The period of investigation, July 5 to mid-September 2019, was characterized by generally increased volcano-seismic activity. INGV reports intensive degassing and ash emissions from NEC in the first week of July (INGV, 2019a, figure 3.1).

Figure 3.1.: Ash plume on July 6, 2019 (photo: Michael Weber)

This was followed by Strombolian explosions and lava flows originating at the NSEC in the days of July 18-20 and 27-28. A continuous increase of the volcanic tremor amplitude was observed from mid-August, peaking on September 12 with the Strombolian eruption at VOR (Eibl et al., 2022; Giuffrida et al., 2021). Further, Sciotto et al. (2022) and Giuffrida et al. (2021) note that tremor and LP event locations during this time were concentrated at shallow depths (>1.5km and >2km a.s.l., respectively) and under the summit crater area. The following figures 3.2 to 3.4 show the locations of tremor events during the period of investigation, reported by the INGV. Locations are derived from the seismic amplitude decay (Cannata et al., 2013; Di Grazia et al., 2006). As was described by both Sciotto et al. (2022) and Giuffrida et al. (2021), they clearly image the migration of volcanic tremor to shallower depths and towards the active eruptive vents.

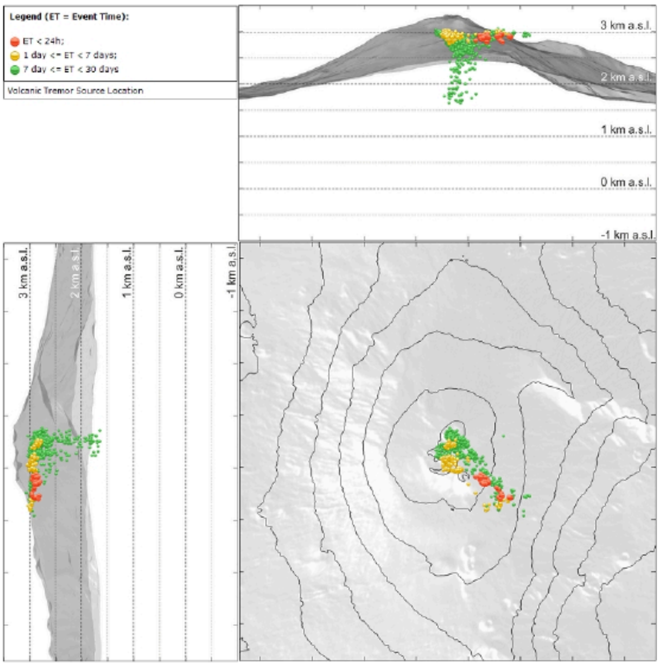

Figure 3.2.: Locations of tremor events June 29 to July 28 (INGV, 2019b)

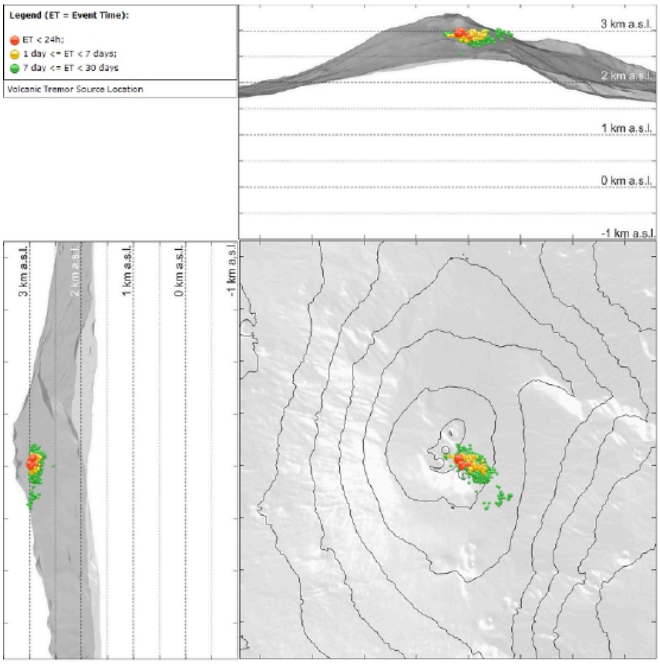

Figure 3.3.: Locations of tremor events July 26 to August 25 (INGV, 2019c)

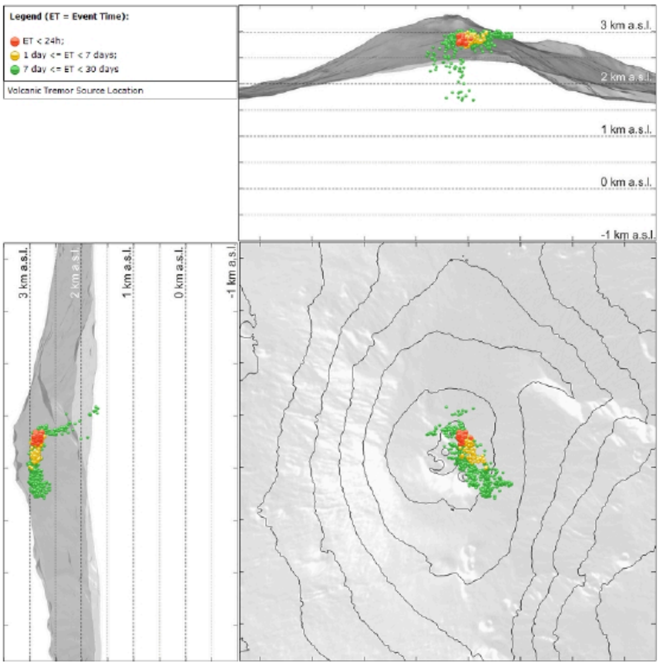

Figure 3.4.: Locations of tremor events August 23 to September 22 (INGV, 2019d)

4. Instrumental Setup and Data

The main dataset used in this study was recorded on a seismic array consisting of 26 broadband stations between July 5 and September 13, 2019. The array was located at the northeastern flank of the Etna volcano near Pizzi Deneri observatory on Piano delle Concazze (PDC), about 2 km from the North East Crater (figure 4).

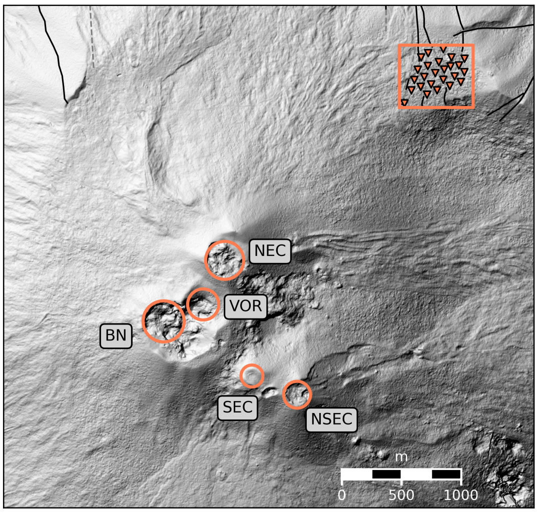

Figure 4.1.: DEM of Etna (from: Palaseanu-Lovejoy et al., 2019) and array location. Rectangle marks the extent of figure 4.3, circles mark the summit craters. NSEC: New South East Crater; SEC: South East Crater; BN: Bocca Nuova; VOR: Voragine; NEC: North East Crater

The deployment was part of an experiment to investigate the performance of a distributed acoustic sensing (DAS) system recording volcanic activity. Hence, the seismic stations were installed alongside an 1.5 km long fibre optic cable connected to a Silixa iDAS interrogator placed in the Pizzi Deneri observatory (Currenti et al., 2021; Diaz-Meza et al., 2023).

All locations of the array were equipped with Trillium Compact 120s sensors, buried at a depth of about 40 cm. According to Foti et al. (2017) buried stations directly on ground is the most desirable setup for the measurement of high-quality ambient noise data. DiGOS DATA-CUBE[3] digitisers recording at a sampling rate of 200 Hz were used for data acquisition. Due to technical problems station BB05 was not recording correctly during most of the experiment. It was therefore excluded from any further analysis. From August 24th on a rotational seismometer was deployed next to station BB17, at the center of the array. Both instruments were set up on a stone plate and not directly on ground as all other stations (Eibl et al., 2022). The interstation distances of neighbouring stations are in the order of 70 to 100 m with the whole set-up covering approximately 0.2 km^2. The area is largely flat so that the elevation of the stations varies between 2795 and 2809 m. More details and exact locations of the broadband stations can be found in Appendix A.

The second dataset used here are the records of the DAS system, encompassing the same timespan. All files were available in the miniSEED format, split according to the channel spacing of 2 m and decimated to 200 Hz.

Figure 4.2.: View over Piano delle Concazze towards crater region of Etna and seismic station (photo: Michael Weber)

PDC is covered by a layer of loose, unconsolidated volcanoclastic deposits of recent volcanic activity (figure 4.2). Underneath, a system of lava flows burrying the northwest rim of the older Ellittico caldera is found (Coltelli et al., 1994; Napoli et al., 2021). These lava flows, originating the crater area were dammed up by the outcropping caldera rim and diverted to the north (Pichler, 1984, see figure B.1).

Tectonically the area is subject to the influence of the north-east rift resulting in a number of north-south trending faults passing through PDC (Azzaro et al., 2012). Figure 4.3 shows the layout of the broadband array, the fibre optic cable and the locations of known exposed and hidden faults in the area.

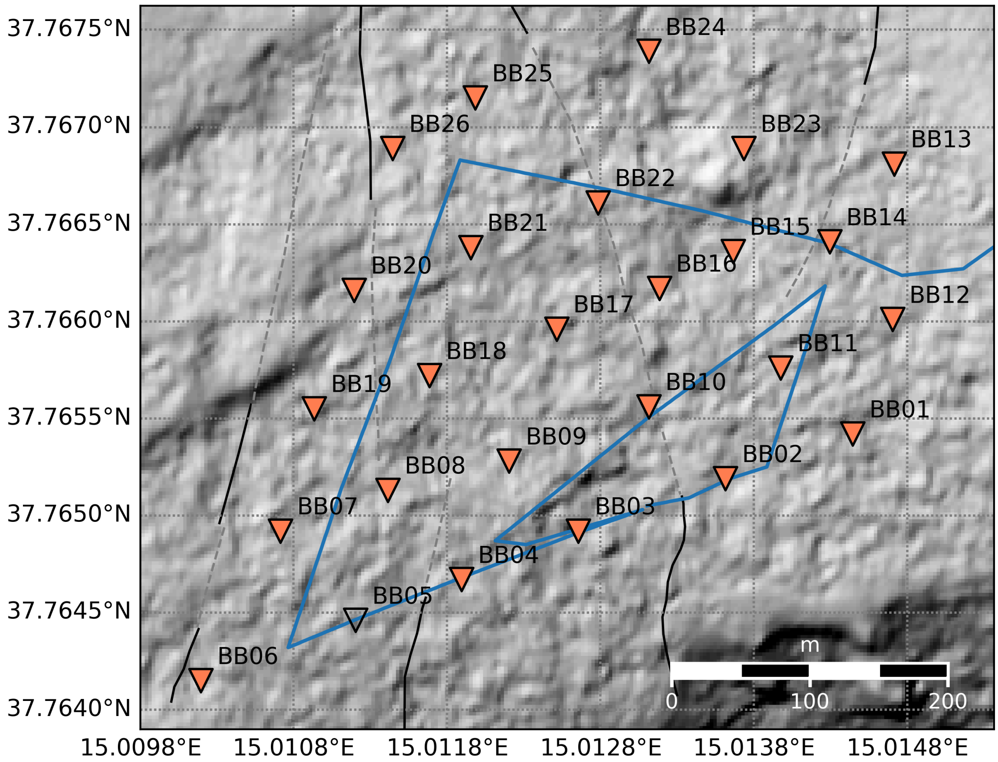

Figure 4.3.: Layout of the seismic array with station names, unfilled triangle marks station BB05; blue line depicts path of the fibre-optic cable; solid black and dashed grey lines indicate exposed and hidden faults respectively (after: Azzaro et al., 2012)

5. Methodology

Chapter 2 described the theoretical background of the two principle methods used in this study. In this chapter the implementation of H/V and SPAC, the software used and the setting of necessary parameters will be presented. Ultimately, the inversion of the results and the derivation of 1D velocity models will be discussed in detail.

Both, computation of HVSRs and SPAC curves for this study have been implemented in python codes. Although compromising on the runtime, compared to tools implemented in other programming languages, this ensures the programs can be read, edited, expanded, reused and integrated with other seismological tools easily. It also allows to make use of a number of efficient and widespread methods and functions developed for scientific computing and working with seismological data. Namely, the computations are based on the *NumPy*, *SciPy* and *ObsPy* packages and visualizations are handled by either *seaborn* or *Matplotlib*. Specific methods and functions will be mentioned in the subsequent sections.

In addition, some modules of the open-source application *Geopsy* (Wathelet et al., 2020) were used. Most importantly, the entire inversion process is handled by the *Dinver* framework (see section 5.3).

Next to H/V and MSPAC fk-analysis was used to track the backazimuth of the volcanic tremor during selected time periods. For this the *array_processing* function of *ObsPy* was utilized.

5.1. Computing H/V ratios

The following points describe how the individual processing steps for the computation of HVSRs were implemented:

- **Definition of parameters and data**: First the data to process and some parameters need to be defined, the optimal selection of which depends on the dataset:
    - **window length**: the length of a single time window
    - **time range and dates**: the time over which individual windows are later averaged and how often this is repeated
    - **frequency range**: the frequency range in which to compute the H/V curve
    - **inventory and data**: the *ObsPy*-inventory object containing the metadata of stations and the location of data
- **Loading data**: The data for the defined time range is detrended and loaded into an *ObsPy* stream.
- **Slicing to window size and station selection**: The stream is sliced according to the defined window length and the data of a single station is selected.
- **Anti-triggering**: To avoid the processing of transient events, a STA/LTA-trigger is applied to the data. In case of a detection, the data is rejected and the next station will be selected.
- **Tapering**: In order not to distort the results of the following transformation into frequency domain, a taper is applied to the data by multiplication of each components record with a cosine-tapered or Tukey window. This constitues the most commonly used tapering function in seismic noise processing (Pilz & Parolai, 2012). The shape parameter is set to 0.1, meaning that 10% of the data is inside the tapered region. The window is provided by the *tukey* function of the *SciPy* package.

- **Compute spectra**: The one sided FAS is computed for all three components. Here *NumPy*'s functions *rfft* and *rfftfreq* are used.
- **Smoothing of spectra**: The spectra are smoothed by using the method proposed by Konno and Ohmachi (1998) which is implemented in *ObsPy*'s *konno_ohmachi_smoothing* function. The bandwidth parameter is set to 40 samples.
- **Averaging of horizontal spectra**: The RMS of both horizontal spectra is determined.
- **Compute H/V**: The H/V ratio is computed by dividing the averaged horizontal spectrum by the vertical. Then, the frequency corresponding to maximum HVSR is found and both results are stored.
- **Loop over stations and time windows**: The process is repeated for all stations in the inventory before continuing with next time window. Stations and times where no data is available are stored.
- **Average over all time windows**: Finally the average H/V curve and peak frequency of all time windows is calculated for each station together with the corresponding standard deviations.
- **Save final results**: The final results and standard deviations are stored into a python object. For future access, the object is also written to the computer using python's *pickle* module.

SESAME (2004) gives an extensive guideline on the H/V technique. The authors define multiple criteria as to when a HVSR curve can be considered reliable, amongst others these are: (1) $f_0 > \frac{10}{l_w}$ and (2) $l_w * n_w * f_0 > 200$, with l_w being the window length and n_w the number of windows. Further, for $f_0 \approx 0.5$ Hz a recording time of 20 minutes, a minimum window length of 20 seconds and a minimum number of 10 windows is recommended.

Based on these criteria and the amount of data that is available, a window length of 30 seconds and a total time of one hour that is being processed was chosen. With respect to the spectral characteristics of the present volcanic tremor (section 3.2), the frequency band between 0.5 and 12 Hz is investigated. This choice ensures to include the expected fundamental frequency of the site and possible secondary peak frequencies.

STA and LTA windows are 2 seconds and 20 seconds respectively, the trigger threshold is set to 4. However, it has been shown that the processing of transient signals does not worsen the HVSR result noticeably (Parolai & Galiana-Merino, 2006).

5.1.1. Combined seismometer and DAS HVSRs

As demonstrated in Spica et al. (2020), HVSRs can be computed from the combination of DAS and broadband data to assess site effects with much higher spatial resolution than with traditional seismic arrays. This includes the conversion from the strain-rate records of the DAS to velocity data. Here a more simple approach is chosen to extract additional subsurface features. The two merged horizontal spectra H_S in equation 2.1 are replaced by the spectrum of a single DAS channel. The vertical spectrum is computed from the broadband station that is closest to the respective DAS channel. This is possible since the vertical velocity component is generally more spatially stable (Spica et al., 2020, and references therein).

The strain-rate data is not converted to velocity but simply integrated so that the resulting HVSR is composed of a strain data spectrum and a velocity data spectrum. This allows to include DAS records easily in the described HVSR computation and with very little adaption of the program's code. For this work strain-rate data of 690 channels is available. For each channel the record first is integrated and the nearest broadband station is found. The corresponding time series are then processed as described before. In total, 50 60 s time windows were processed and averaged.

5.2. Deriving autocorrelation curves with SPAC

The following points describe how the individual processing steps for the computation of the SPAC curves were implemented:

- **Define and edit inventory**: An ObsPy inventory of the array to be used must be provided. The array and the corresponding co-array will be plotted. Stations to be excluded from the analysis can be given and will be removed from the inventory. A central reference station can be given, else all possible station pairs in the array will be used.

- **Define rings, data and processing parameters**: Based on the co-array plot, MSPAC rings can be set by providing r_1 and r_2 for each ring. Rings are plotted and the number of station pairs per ring is computed, so that selection can be optimized.

  Further, the following inputs need to be provided:

  - **Frequency band**: The range of frequencies in which SPAC will be computed
  - **Number of center frequencies**
  - **Shift**: The maximum time shift for the correlation
  - **Data**: The data to be processed
  - **Times**: The time windows of the data to be processed. This can either be a list of *DateTime* objects giving starttimes and endtimes or a starttime, window length and number of time windows

- **Generate list of station pairs**: Using the inventory to generate a list of all station pairs, if provided, only station couples with reference station are considered.

- **Generate center frequencies**: The center frequencies are generated by spacing them evenly along a logarithmic scale in the given frequency band.

- **SPAC computation**: The following steps are then repeated for each station pair in the list:
    - **Compute the distance and azimuth between both stations**
    - **Rotation**: Horizontal components are projected into radial-transverse coordinate system, using the computed azimuth value.
    - **Filtering and correlation**: The data stream is filtered by a four corner bandpass filter with passband between 0.9 and 1.1 times the center frequency. The corresponding components are correlated, time lag and amplitude of the correlation functions maximum is stored. This is then repeated for all center frequencies.
- **Averaging**: According to the ring selection, processing parameters and equation 2.16, first the weighted azimuthal average and then the time average over all windows is computed.
- **Display of result**: The final result can be displayed together with the theoretical autocorrelation curves for a user-provided velocity model. The synthetic curve is given by the *Geopsy* forward modelling routine.

For this study 80 time windows of 60 seconds length with 50% overlap were processed. The maximum shift was set to 10 seconds and the SPAC coefficient was computed for 100 center frequencies.

5.2.1. Ring selection and frequency range for MSPAC

The selection of the ring's number and radii is a tradeoff between the number of station pairs per ring and its thickness. The first should ensure a good azimuthal resolution while the latter should be as thin and therefore as close to an ideal circular sub-array as possible. It was however found, that azimuthal resolution is much more important to derive a meaningful result than the width of a ring (Köhler et al., 2007).

Thanks to the large number of available stations and corresponding station pairs, rings could be chosen relatively thin, i.e. in the range of a few tens of meters. The following table shows the selection of MSPAC rings for this study, figure 5.1 the corresponding co-array plot:

Ring	r_1 **[m]**	r_2 **[m]**	$n_{stations}$
1	45	60	8
2	60	75	25
3	75	90	19
4	90	105	8
5	105	120	13
6	120	132	19
7	132	145	24
8	145	178	44
9	178	200	41
10	200	215	15
11	215	250	41
12	250	300	33

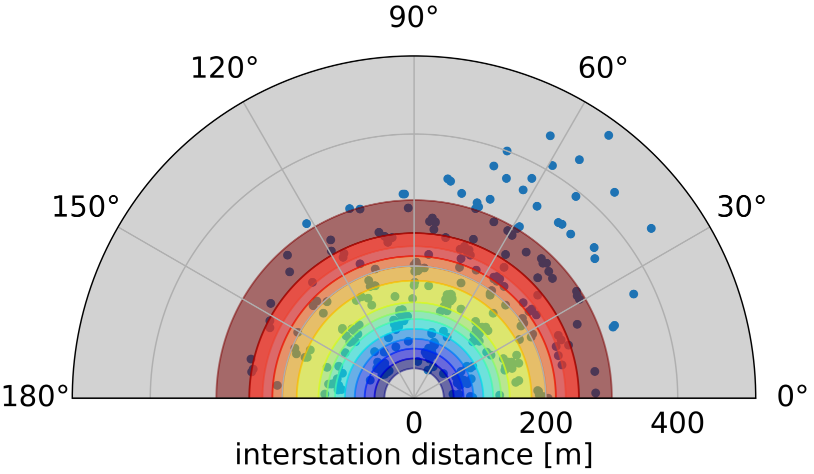

Figure 5.1.: Chosen MSPAC ring distribution in co-array plot

It has been shown that reliable SPAC curves can be obtained for wavelengths shorter the

often assumed $2r \leq \lambda$ (Cho, 2022; Tsai & Moschetti, 2010). Therefore, SPAC curves are first computed between 0.5 and 3 Hz, thus encompassing most of the frequency range of the volcanic tremor and later cut to a suitable bandwidth.
In accordance with other studies, all curves are inverted under the assumption that only the fundamental modes of the surface waves are contributing to the investigated frequency band (e.g., Di Giulio et al., 2009; Saccorotti et al., 2004).

5.3. Inversion

As mentioned, the process of inverting the gained results for 1D shear wave velocity models is done using the *Dinver* framework of *Geopsy*. *Dinver* is a C++ implementation of the neighbourhood algorithm (NA; Sambridge, 1999), improved by Wathelet (2008). It is not limited to any specific inversion problem, but can be used with any external forward computation that is provided. Here, the plugin *dinverdc* is used that is developed for the inversion of surface wave data.
For this analysis the H/V peak frequencies and the SPAC curves will be inverted jointly. It has been shown that the results from both methods contain complementary information: HVSR peaks constrain the thickness of the subsurface layer well, while the autocorrelation curves give information on the absolute v_S-values in depth (e.g., Ikeda et al., 2013; Parolai et al., 2005; Scherbaum et al., 2003; Spica et al., 2018). The forward computations, especially for the HVSR curve, are beyond the scope of this thesis, they are discussed in detail in Wathelet (2005).

In order to evaluate the performance of a single model generated in the inversion process, a misfit or objective function needs to be defined. The misfit for the H/V frequency peaks is simply given as:

$$misfit_{f_0} = \frac{|f_{0,obs} - f_{0,calc}|}{\sigma_{f_{0,obs}}} \tag{5.1}$$

$f_{0,obs}$ and $f_{0,calc}$ are the observed and the calculated H/V peak frequencies and $\sigma_{f_{0,obs}}$ is the standard deviation of $f_{0,obs}$.

Conventionally the derivation of v_S profiles from SPAC curves was carried out by first deriving the DC using a least-squares approach and then inverting the DC for the velocity distribution. As Wathelet et al. (2005) describes, this two stage process can be merged into a single inversion, so that results can be obtained from the SPAC curves directly. For a given velocity model, the DC is computed and the theoretical SPAC is then found by the application of equation 2.13 and the equivalents for the horizontal components. The corresponding misfit function is defined as a RMS value, normalized by the standard deviation of the data points:

$$misfit_{SPAC} = \sqrt{\frac{1}{\sum_{k=1}^{n_R} n_{Fk}} \sum_{i=1}^{n_R} \sum_{j=1}^{n_{Fi}} \frac{(\rho_{dij} - \rho_{cij})^2}{\sigma_{ij}^2}} \tag{5.2}$$

where ρ_{dij} is the SPAC coefficient of the data, ρ_{cij} is the calculated SPAC coefficient each at frequency f_j and the ring i, σ_{ij}^2 is the corresponding observed variance, n_R is the number of rings and n_{Fi} is the number of frequency samples for ring i. In case of a joint inversion, both misfit functions are combined so that the global misfit function is:

$$misfit_{global} = (1 - \varepsilon)\ misfit_{SPAC} + \varepsilon\ misfit_{f_0} \tag{5.3}$$

where ε is a weighting parameter ($0 < \varepsilon < 1$).

Testing different ε values showed that weighting steers the result of the inversion heavily towards only fitting either the HVSR peak or the SPAC curves. As there is no *a priori* information on the reliability or quality of either, both HVSR and SPAC curves are weighted equally in this study.

5.3.1. Neighbourhood algorithm

The neighbourhood algorithm is a direct search algorithm to explore a multidimensional parameter space and find models of appropriate data fit. Instead of giving the single best fitting model, it is designed to find an ensemble of models sampling all equivalent minima of the misfit function. The NA is not using derivatives and explores the parameter space globally, which is essential due to the high degree of non-uniqueness of the problem. Using a Monte Carlo technique, it is based on the generation of pseudo-random samples. In this regard, it can be compared to simulated annealing or genetic algorithms (Sambridge, 1999).

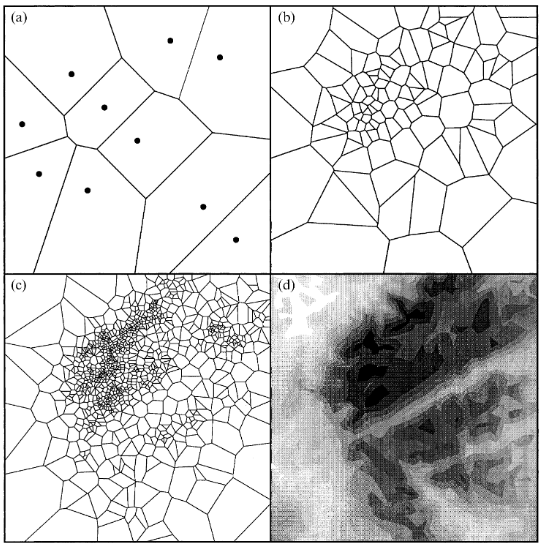

Figure 5.2.: 10, 100, and 1000 samples with their Voronoi cells (a-c) and contour of the misfit function (d); note the shift of sampling density and how multiple minima of the objective function are explored (from: Sambridge, 1999)

In a first step, a number of inital random samples, i.e. sets of model parameters, are generated. For each sample the forward computation is executed and the result is compared to the observed data, resulting in a misfit value. From these initial forward computations the surface of the misfit function can then be approximated. The parameter space is divided into Voronoi polygons and each cell is assigned the misfit value of the corresponding sample as a constant value. Now, the most ”promising” areas of the parameter space, that is the ones with the lowest misfit, are resampled by again generating random samples inside the boundaries of the Voronoi cells and the process repeats. This way, the samples already evaluated are guiding the algorithm into exploring all minima of the objective function effectively. Figure 5.2 illustrates this process for a two-dimensional parameter space.

In the NA implementation used here, there are three key tuning parameters to govern the behaviour of the algorithm.

- the total number of models to generate by NA in one inversion run (N_s)
- the number of models to generate randomly by MC sampling (N_{s0})
- the number of cells to resample per iteration (N_r)

Here, both N_{s0} and N_r are set to 100, which according to Wathelet (2005) is typical for a more explorative approach. This then requires a greater number of total generated models to still sample all local minima appropriately dense. Testing showed that a N_s of 10000 is more than enough to infer a stable misfit value (see figure 5.3). Further, due to the random component of the NA, Wathelet et al. (2005) state that it is necessary to repeat the inversion process three to five times to ensure a robust final inversion result.

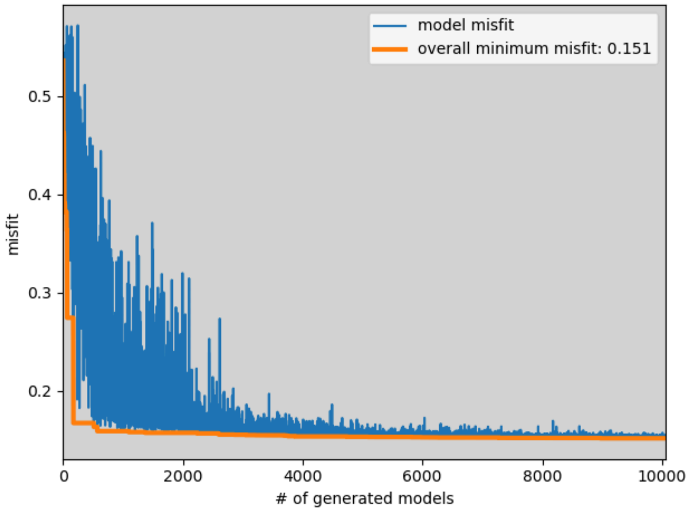

Figure 5.3.: Exemplary misfit evolution for one inversion run with $N_s = 10000$; a sufficiently stable misfit value is reached after 4000 to 5000 evaluated models

5.3.2. Parameterization and *a priori* information

Renalier et al. (2010) demonstrated the non-uniqueness of this inverse problem and the drastic influence parametrization has on the estimated velocity distribution. A carefully chosen parameterization therefore is essential for obtaining robust and meaningful results.

Here, a layer of an 1D velocity model is characterized by four parameters, namely compressional and shear wave velocity (v_P, v_S), density (ϱ) and the layer thickness (h). Xia et al. (1999) and Wathelet (2005) analyzed the sensitivity of the DCs shape to these parameters. They found that v_S is by far the most dominant parameter. In contrast, the influence of ϱ is negligible and the influence of v_P is significant only for low Poisson's ratios which are not to be expected in the loose and unconsolidated material present at the investigated site. Consequently, resulting P-wave and density profiles should not be interpreted and if possible, values can be assigned as constant. For the density this could be confirmed during a few test runs of the inversion with ϱ as a free parameter. As figure 5.4 shows, no clear correlation between the model misfit and the ϱ-value is visible. Since Jousset et al. (2022) give a measured value of 520 ± 10 $\frac{kg}{m^3}$ for the surface scoria at the site, the density parameter was therefore fixed at 520 $\frac{kg}{m^3}$.

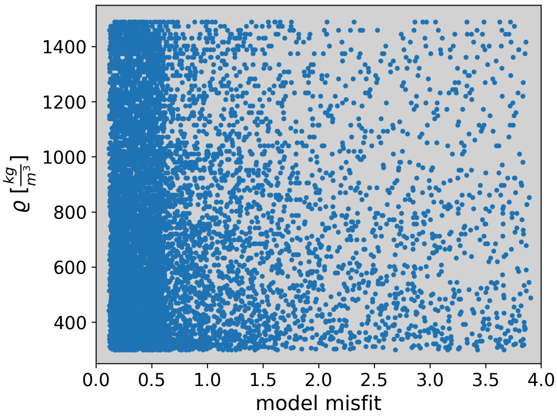

Figure 5.4.: Model misfit for different density values of the 500 best models produced in one inversion run

For the v_P profile a very simple parameterization is chosen, i.e. a single layer over half-space. In order to avoid influencing the resulting v_S profile by fitting any too tight constraints put on v_P, the possible values are given very wide boundaries. This is following the findings of Wathelet (2005) for the case where no prior estimate or data of v_P is available. Additionally, to better constrain the inversion result, more conditions are introduced:

- **no low velocity zones**: The seismic velocities increase with depth, i.e. a layer's velocity is always higher than the velocity of the layer above.
- **Poisson's ratio**: As discussed, v_P profiles are not well recovered and will therefore not be interpreted. However, results should be physically realistic, so that v_P and the corresponding v_S value at the same depth are linked by ν with $0.2 < \nu < 0.5$.
- **bottom depths**: The bottom depth (d) of the surface v_P layer must be the same as the bottom depth of one of the layers in v_S.

As the number of v_S layers is unknown, the approach is to start with a single layer over half-space and successively adding layers while observing the misfit value. This avoids overparameterization while guaranteeing a sufficiently high number of layers, as too few can lead to an overestimation of the impedance contrast (Scherbaum et al., 2003). Here no misfit decrease could be see for inversions with more than two layers over the half-space.

Foti et al. (2017) gives a maximum depth resolution for the SPAC of $d_{max} \leq \frac{\lambda_{max}}{2}$, with λ_{max} being the maximum resolvable wavelength. Taking into account the interstation distances of the array and the expected low phase velocities of the medium, d_{max} is estimated to be ≈ 90 m. The final model parameterization is shown in the following table:

v_P			v_S			ϱ	ν
Layer	**Vel.** [$\frac{m}{s}$]	**d** [**m**]	**Layer**	**Vel.** [$\frac{m}{s}$]	**d** [**m**]	[$\frac{kg}{m^3}$]	
0	150 - 3000	d($v_{S,1}$)	0	50 - 400	1 - 40	520	0.2 - 0.5
half-space	200 - 3000	∞	1	50 - 800	20 - 70		
			half-space	300 - 800	∞		

6. Results

In this chapter the obtained results will be presented. After briefly investigating the temporal evolution of the H/V spectral ratios, the detailed analysis of a suitable time sample will be shown. The spectral ratios and the spatial distribution of peak frequencies are shown and finally the inferred SPAC curves and the inversion result will be given.

6.1. Temporal evolution of HVSRs

Figure 6.1 shows the H/V peak frequency values for each station averaged over one hour from July 5 to September 12, the corresponding standard deviations (σ) are shown in figure 6.2. It can be seen that large periods show a strong variability of f_0 over time and high σ values.

Abrupt changes and high variability in H/V ratios coincide with increased volcanic activity. Exemplary this can be shown comparing f_0 values and RMS tremor amplitude records published by INGV from July 27 (figures 6.5 and 6.3). The drastic increase in tremor amplitude concurs with a clear change in HVSRs in the early hours of the day.

Further, fk-analysis reveals that during non-eruptive periods most seismic energy is reaching the array from a range of angles encompassing the whole crater region, between approximately 200° and 235°. However, during times of eruptive activity the dominant source region is very stable, with the BAZ pointing to the corresponding active crater and only varying by a few degrees (see D.1).

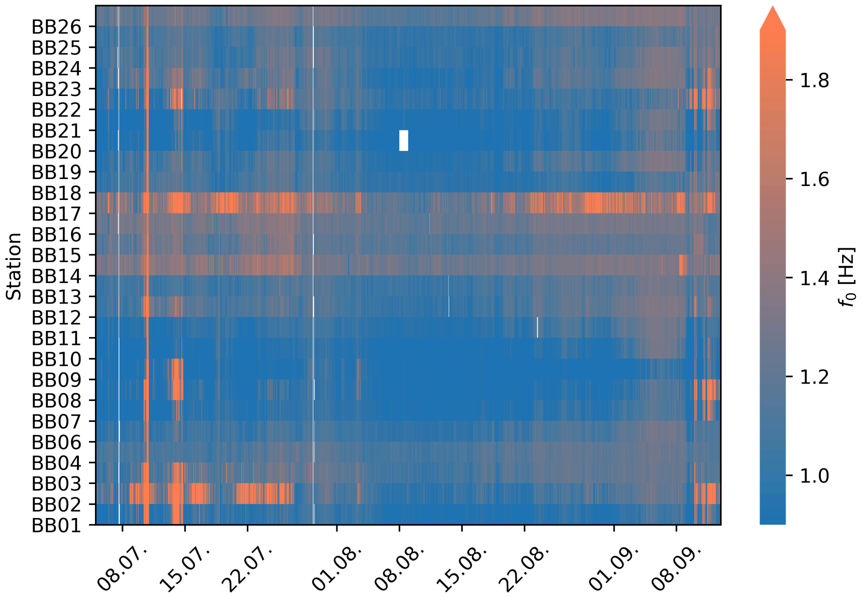

Figure 6.1.: All f_0 values averaged in one hour bins from July 5 to September 12 on the 25 seismic stations

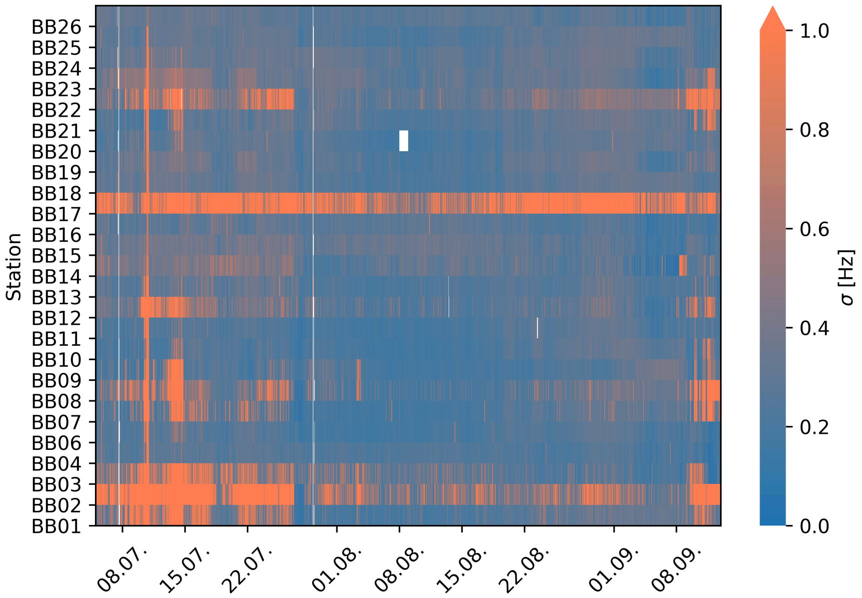

Figure 6.2.: The corresponding σ values of the H/V peak frequencies in figure 6.1

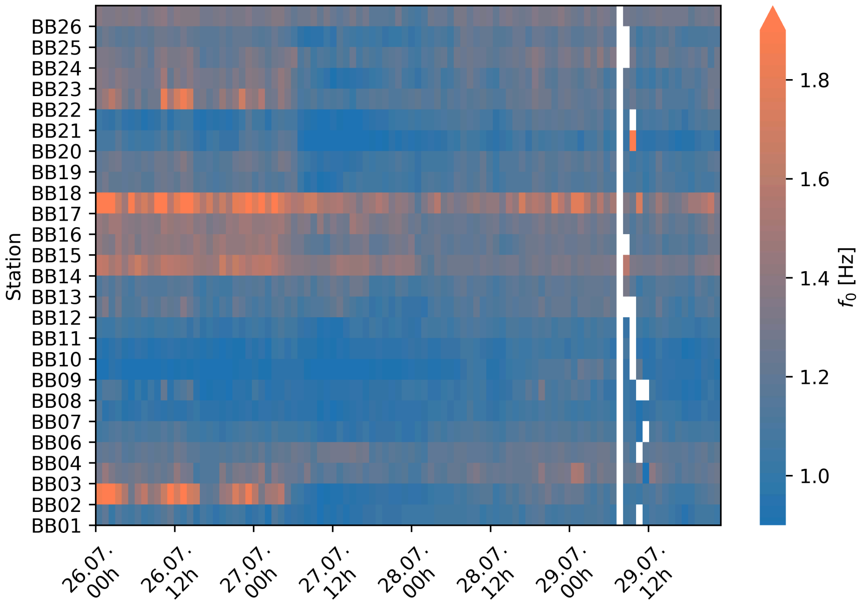

Figure 6.3.: f_0 values averaged in one hour bins from July 26 to 29; note the abrupt change in peak frequency in the early morning of July 27

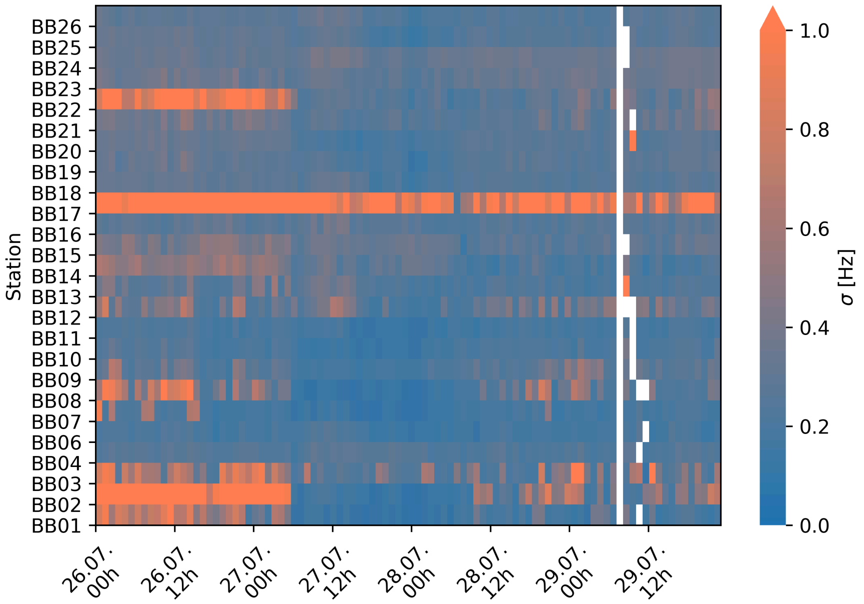

Figure 6.4.: The corresponding σ values of the H/V peak frequencies in figure 6.3

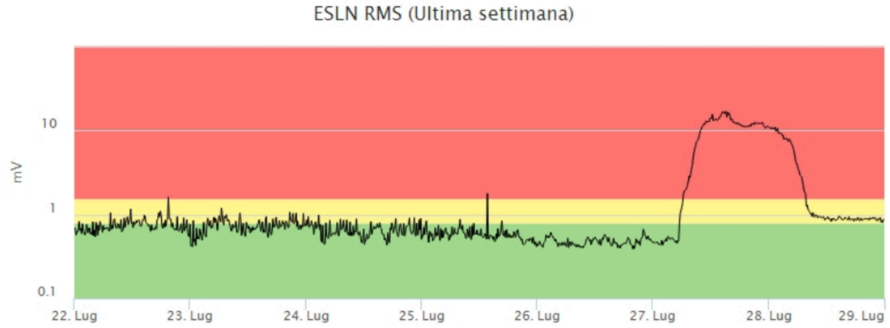

Figure 6.5.: RMS tremor amplitude between July 22 and 29; clearly visible is the increased amplitude from the early hours of July 27 to midday of July 28 (from: INGV, 2019b)

Inspection of the complete HVSRs for multiple time samples shows that only few stations exhibit clear frequency peaks with large σ_f values during periods of increased volcanic activity (see figure C.1).

The predominant source region indicated by the fk-analysis is strongly violating the basic assumption of uniformly distributed sources, making times of increased volcanic activity not ideal for the application of SPAC either. Another example of the correlation between changing H/V ratios, f-k analysis and eruptive activity can be found in D.2.

Hence, it is necessary to identify time periods suitable to infer meaningful HVSRs and spatial autocorrelation curves. This was approached by: (1) visual inspection of all HVSRs and standard deviations (figures 6.1 – 6.3), (2) comparison to INGVs reported RMS tremor amplitude measurements (e.g., figure 6.5) and reports of volcanic activity, (3) f-k analysis results (e.g., D.2, D.4) and (4) the computation of the mean H/V ratio over all stations (figure 6.6).

As can be seen from figure 6.6 the time period around August 8 shows the most stable mean H/V value for the array. It was therefore decided to use this part of the available data for further analysis. This choice also avoids the time of continually increasing tremor amplitude beginning in mid-August and leading up to the September 12 eruption at VOR as described in chapter 3.2.

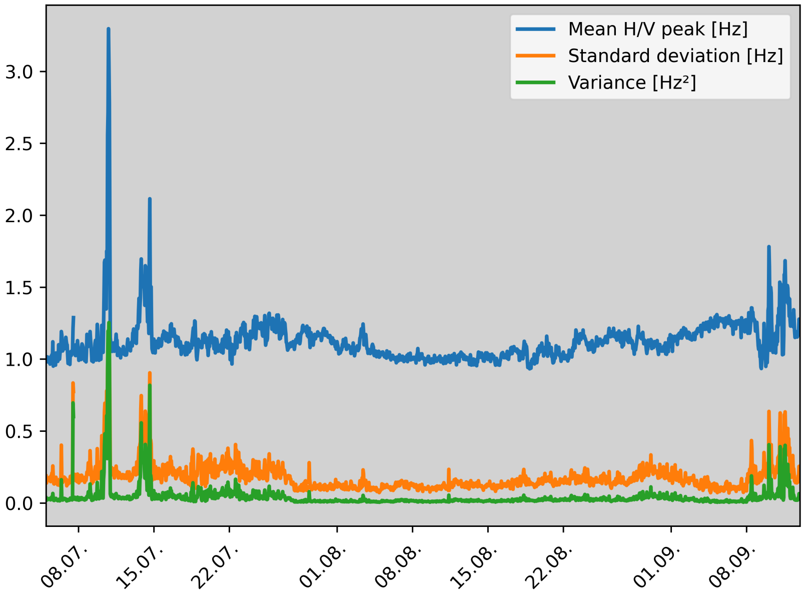

Figure 6.6.: Mean H/V peak frequency over all 25 seismic stations with corresponding standard deviation and variance

6.2. Spatial distribution of HVSR peak frequencies

Figure 6.7 shows the full HVSR curves with their standard deviation σ_A for all 25 investigated stations in a selected 1 hour time window. The legend indicates the corresponding f_0 values and their standard deviation σ_f.

The exhibited HVSR peak frequencies range between approximately 0.8 and 1.3 Hz. Stations with $f_0 < 1$ generally show more clear H/V peaks and lower σ_f with values between 0.15 to 0.2 Hz. In contrast, HVSRs with higher peak frequencies ($f_0 \geq 1.1$) display higher standard deviations of f_0 in the range of 0.20 and 0.47 Hz. The corresponding peaks are generally lower and broader. Specifically, this is the case for the stations BB01, BB06, BB11 to BB15, BB23 and BB24.

Too broad peaks can generally be adressed by changing the bandwith parameter of the smoothing algorithm, however this approach had no noticeable effect on the obtained spectral ratios.

Additionally, the three northernmost stations of the array BB24 to BB26 exhibit small secondary peaks around 5 to 6 Hz.

On all stations the standard deviation of the HVSR amplitude σ_A decreases towards higher frequencies. Around the peak frequencies, the curves exhibit σ_A values between approximately 0.5 and 1.4, where low values are often attributed to lower peak amplitudes.

Very similar results in terms of HVSR shape, absolute f_0 values and their spatial distribution to the one presented here can be inferred from other time samples of the chosen range of days. However, some results show significantly higher standard deviations.

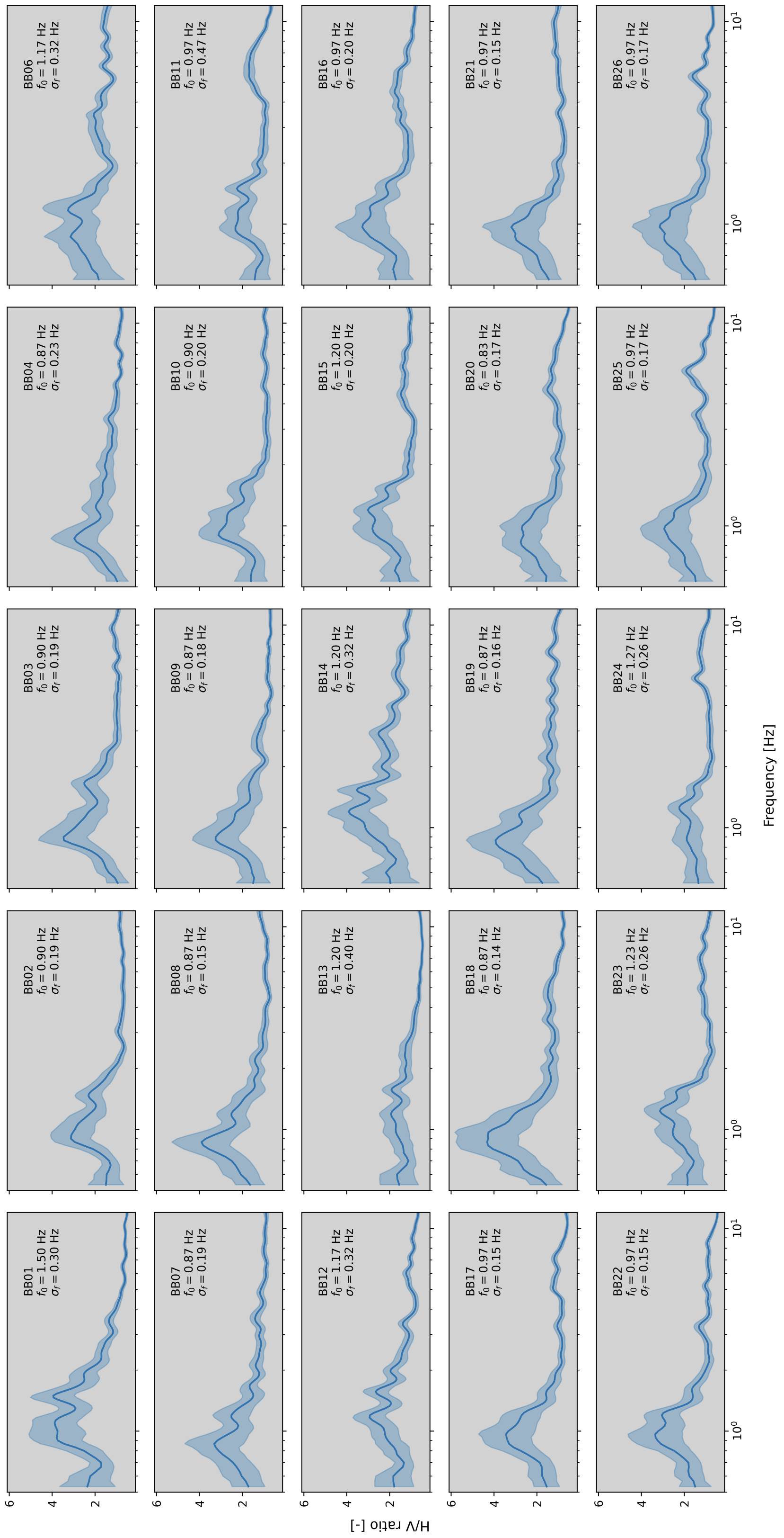

Figure 6.7.: All station's HVSRs from August 9, 21 h; light blue area marks standard deviation (σ_A)

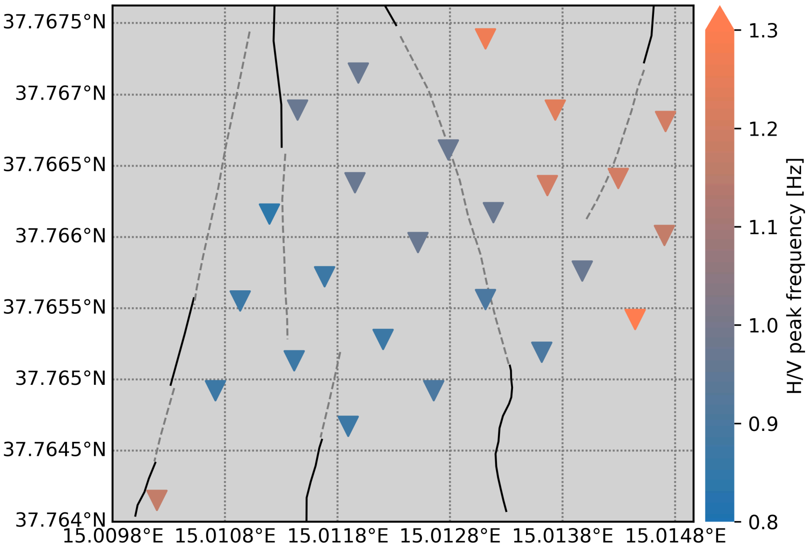

Figure 6.8.: Spatial distribution of f_0

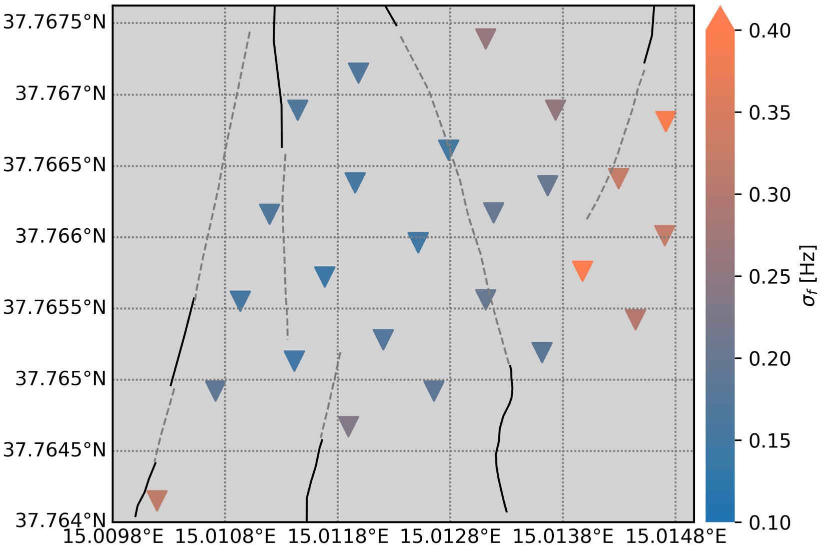

Figure 6.9.: Spatial distribution of σ_f

Figure 6.8 shows the spatial distribution of the H/V peak frequencies. A clear trend towards higher f_0 going from the southwest to the northeast of the array is visible. The aforementioned stations with high f_0 are all located in the northeastern part of the setup, only BB06 is located in the very southwestern corner.

Accordingly, the same southeast-northwest trend can be seen in the spatial distribution of σ_f (figure 6.9). Lastly, the inferred peak frequencies were interpolated on a 100 by 100 node regularly spaced grid using a cubic spline interpolation. Figure 6.10 shows the resulting map. The interpolated result indicates a sharp transition from the area of higher (> 1.1) f_0 in the northeast to lower (< 1) f_0 in the southwest and center of the layout. In the northern half, this shift coincides roughly with the fault crossing through the array.

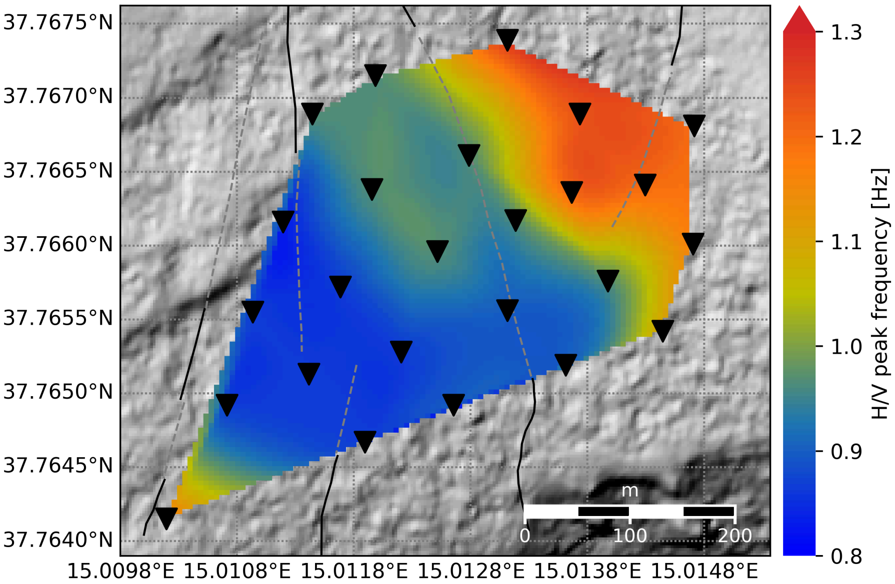

Figure 6.10.: Interpolated spatial distribution of f_0

6.2.1. Combined seismometer and DAS HVSRs

Figure 6.11 depicts the maximum amplitude of the HVSR $A_{H/V}$ for each of the 690 DAS channels. Areas of strongly elevated values coincide with the present faults. This is especially clear for the two buried faults crossed by the cable in the north and the fault crossed in the southwest. No significant effect on the H/V amplitude is visible for the western fault. Other areas of higher amplitudes on the eastern cable loop do not fall together with the mapped faults.

Figure 6.12 shows the full shape of the H/V curves for the channels 190 to 280, spanning the area of the two faults the cable crosses on the northern straight. Clearly elevated amplitudes coinciding with the faults are visible. West of the eastern fault and east of the western fault, the curves are almost completely flat. In the middle between both faults, amplitudes are again slightly higher and form a double peak.

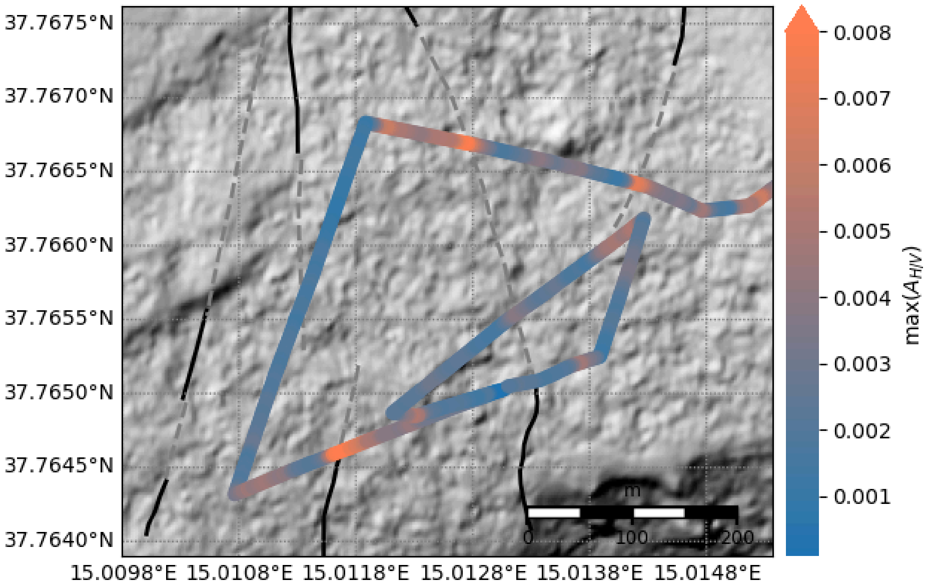

Figure 6.11.: Maximum amplitude of H/V curves for combined broadband and DAS HVSRs; range of values is due to different units of processed records

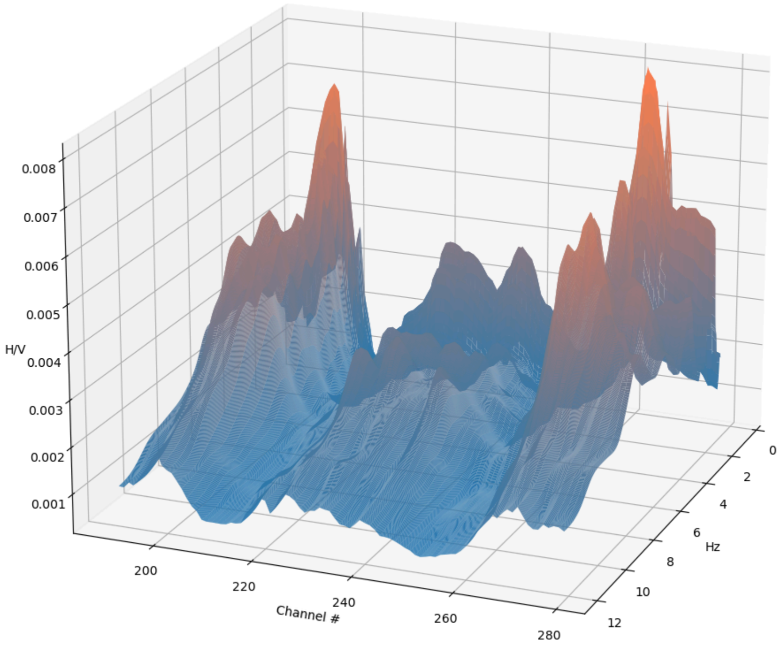

Figure 6.12.: Shape of HVSR curves for channels 190 to 280

6.3. SPAC results

Figure 6.13 shows the SPAC curves for all 12 rings and their respective standard deviations. The orange line represents the theoretical curve for the velocity model given in Punzo et al. (2011).

For all three components the begin of the Bessel curves's arc is visible on most of the MSPAC rings. With increasing ring dimensions, the frequency band exhibiting significant values becomes narrower and is shifted to lower ω. For higher frequencies, the curves approach zero. On rings 1 to 4 the obtained curves agree well with the chosen theoretical comparison roughly between 1 and 1.7 to 2 Hz. Standard deviations are consistently around 0.2 and generally lower for higher frequencies.

Due to the very limited suitable frequency range on ring 11 and 12, the corresponding curves were not included in the inversion process.

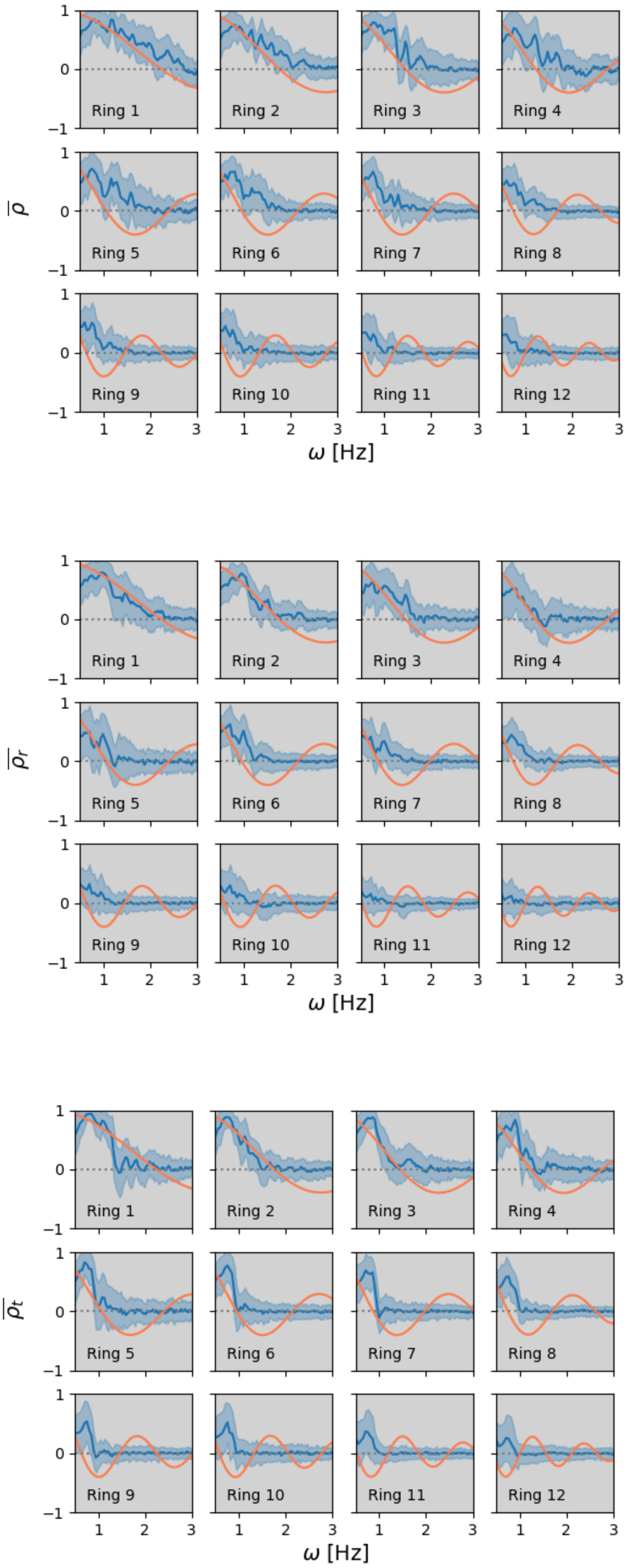

Figure 6.13.: SPAC curves for the vertical, radial and transversal component and the theoretical curve for velocity model of Punzo et al. (2011); light blue area indicates standard deviation of obtained curve

6.3.1. Inversion of SPAC curves only

Figure 6.14 shows the shear wave velocity model with the lowest misfit from the inversion of the three component SPAC curves only. The first interface can be seen at 21.8 m depth and the first layer exhibits a v_S of 165 $\frac{m}{s}$. The second layer with a velocity of 378 $\frac{m}{s}$ ranges down to 65 m where the transition to the half-space and a v_S of 506 $\frac{m}{s}$ is located.

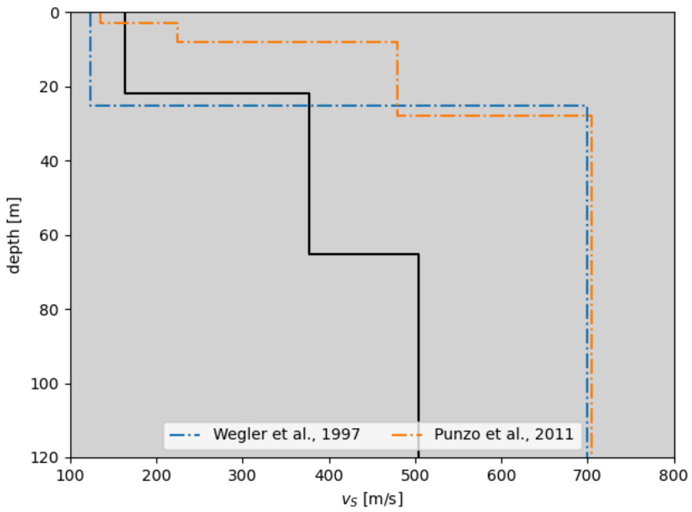

Figure 6.14.: v_S velocity model with lowest misfit together with models from Wegler and Seidl (1997) and Punzo et al. (2011)

Figure 6.15 presents the total misfit evolution during the inversion process. A stable misfit is reached after around 5000 to 6000 generated models with the minimum overall misfit of ≈ 0.149.

The parameter space with model misfits in relation to the individual inversion parameters is shown in figure 6.16. Parameters related to the v_S profile mostly converge towards a stable value, for $d_{S,1}$ the convergence is not as clear. For the two v_P parameters no clear relation between model misfit and velocity is visible.

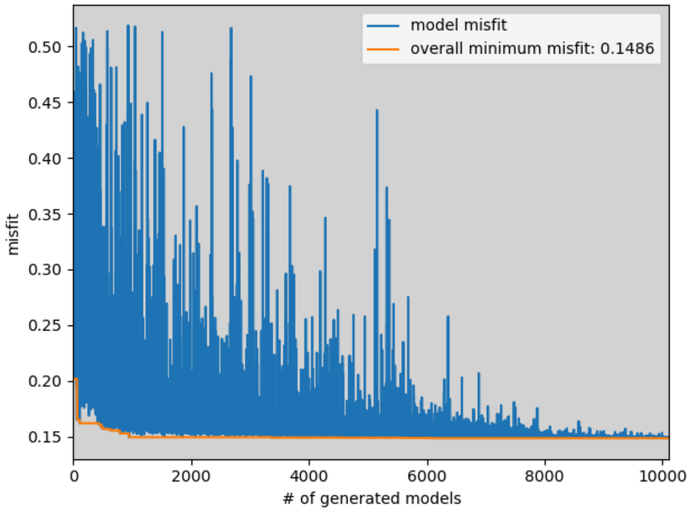

Figure 6.15.: Total misfit evolution for inversion of SPAC curves

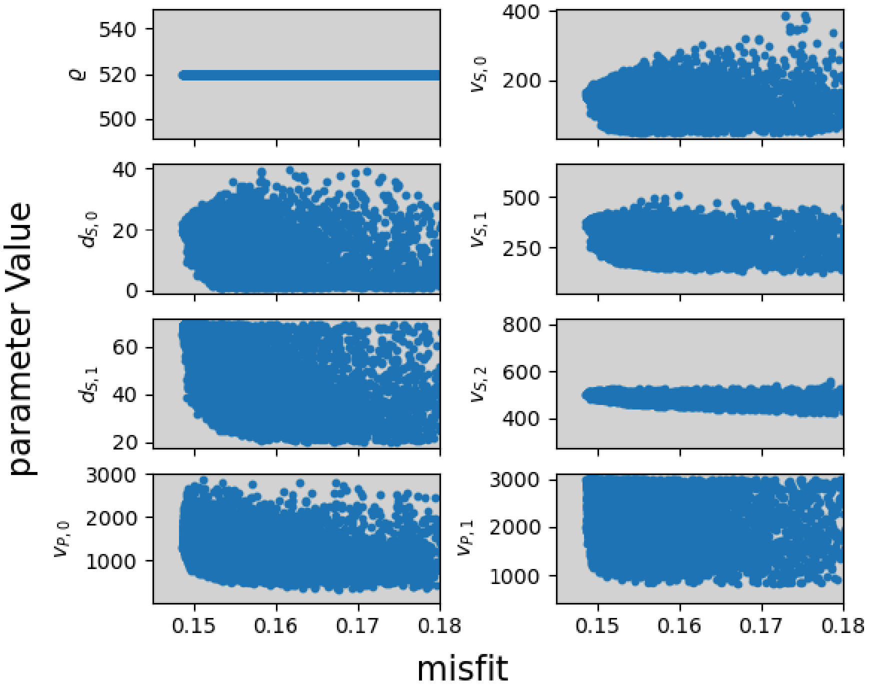

Figure 6.16.: Parameter value and model misfit for the 500 best models

Repeated inversion runs with the same parameterization all yielded almost the same models with misfit values varying by 0.3 to 0.4%.

6.4. Joint inversion

Considering the strong lateral variations in the velocity distribution of the site, a joint inversion using the mean f_0 of the complete array may not produce a meaningful result. Therefore, two separate joint inversions were performed. First, the same parameterization and SPAC curves were used together with a H/V peak of 1.19 Hz and σ_f of 0.05 Hz. This corresponds to the mean peak frequency of the seven stations in the northeastern sector of the array. The second inversion was carried out with a f_0 value of 0.91 Hz and $\sigma_f = 0.05$ Hz, corresponding to the mean peak frequency of the rest of the array. Additionally for the second inversion process, the parameters $v_{S,0}$ and $d_{S,0}$ were fixed at 22 m and 170 $\frac{m}{s}$, respectively. This is due to the good agreement in the properties of the first layer of the SPAC inversion result with the models of Wegler and Seidl (1997) and Jousset et al. (2022) which were obtained at the same site, i.e. in the western part of the broadband array. Figures 6.17 and 6.18 show the results of both inversion processes. The respective misfit evolution and parameter space are given in appendix E.

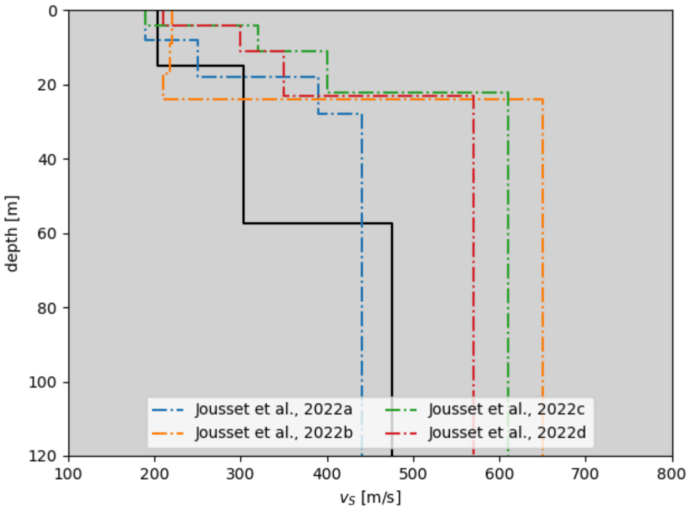

Figure 6.17.: v_S model with lowest misfit for joint inversions with $f_0 = 1.19$ Hz; reference models from Jousset et al. (2022)

In both results, the general shape of the 1D model remains unchanged compared to the simple inversion. For the joint inversion with $f_0 = 1.19$ Hz, the top layer is 7 m shallower and exhibits a higher velocity ($d_{S,0} = 14.7$ m, $v_{S,0} = 203\ \frac{m}{s}$). The second layer's thickness remains constant at 43 m, placing the bottom depth at 57.5 m. Both $v_{S,1}$ and $v_{S,2}$ are lower than in the simple inversion, showing values of 303 and 476 $\frac{m}{s}$, respectively.

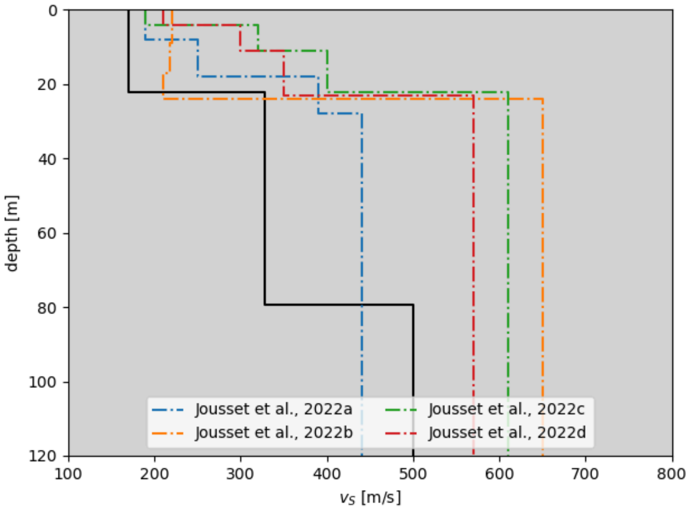

Figure 6.18.: v_S model with lowest misfit for joint inversions with $f_0 = 0.91$ Hz; reference models from Jousset et al. (2022)

The inferred v_S model from the joint inversion with $f_0 = 0.91$ Hz exhibits a thicker second layer with a bottom depth of 80 m. Further, $v_{S,1}$ is slightly lower than for the original inversion (329 $\frac{m}{s}$) and the shear wave velocity of the half-space remains virtually unaltered (504 $\frac{m}{s}$).

With a total minimum misfit of 0.071 and 0.078 the overall fitness of the inversion solution was improved substantially by including the H/V peak frequency. However, for the first joint inversion the results seem to be less stable as a convergence of the individual parameters is less visible. For the second inversion the convergence is much more clear, even for the prior poorly resolved parameters $d_{S,1}$ and $v_{P,0}$.

7. Discussion

In this chapter the obtained results will be discussed and compared to the available scientific literature. Starting, the HVSR curves and their reliability will be estimated and the large temporal variations of the results are being adressed. Then, a brief geological interpretation will be given. Following, the SPAC curves and the inversion results will be discussed and compared to published velocity models.

7.1. HVSRs

SESAME (2004) presents a set of criteria to evaluate the results of HVSR computations. For the whole H/V curve these are the following:

1. $f_0 > \frac{10}{l_w}$
2. $l_w n_w f_0 > 200$
3. $\sigma_A(f) < 2$ for $0.5 f_0 < f < 2 f_0$ if $f_0 > 0.5$ Hz

Here l_w denotes the window length and n_w the number of windows.
As mentioned in section 5.1, l_w and n_w are chosen such that the first two criteria are always met, even when time windows are rejected by the STA/LTA trigger. The third criterium is fulfilled on all stations over the complete frequency range with a maximum σ_A of approximately 1.4. The obtained HVSR curves are therefore valid with respect to the conditions of SESAME (2004).

For the realiability of the H/V peak, the following criteria are given, five of which should be fulfilled to be considered a ”clear” peak.

1. $\exists f^- \in \left[\frac{f_0}{4}, f_0\right] : A_{H/V}(f^-) < \frac{A_0}{2}$
2. $\exists f^+ \in [f_0, 4f_0] : A_{H/V}(f^+) < \frac{A_0}{2}$
3. $A_0 > 2$
4. $f_{peak}\left[A_{H/V}(f) \pm \sigma_A(f)\right] = f_0 \pm 5\%$
5. $\sigma_f < \epsilon(f_0)$
6. $\sigma_A(f_0) < \theta(f_0)$

A_0 and $A_{H/V}(f)$ demark the H/V amplitude at f_0 and f, ϵ and θ are defined as:

- $\epsilon = 0.15 f_0$ and $\theta = 2.00 f_0$ for $0.5 < f_0 < 1$ Hz
- $\epsilon = 0.10 f_0$ and $\theta = 1.78 f_0$ for $1.0 < f_0 < 2$ Hz

The first condition is met for most of the stations. Only the two located most north eastern, BB13 and BB24, do not fulfill the condition clearly. BB20 and BB16 do not meet the criterium but with only very small deviations. Criterium 2, 3 and 6 are fulfilled for all curves. The results of BB01, BB18, BB25 and BB26 fail to satisfy condition 4, while criterium 5 is not fulfilled on all of the available stations.

Although not meeting all the SESAME (2004) criteria, the obtained f_0 peaks can still be considered reliable taking into account that more recently authors have been arguing for wider ranges in criterium 4 and the complete disregard of criterium 5 (Molnar et al., 2022, and references therein).

The relatively large standard deviation values were to be expected as significant temporal variations could already be seen in the full H/V results (chapter 6). The constantly changing and complex nature of the tremor wavefield at Etna and its influence on the spectral ratios have been discussed in a number of publications. Further, the observed

H/V peak frequencies are generally in good agreement with the available literature too. Eibl et al. (2022) describes a change in content of SH and SV type waves in the tremor wavefield during August and September 2019. Patanè et al. (1994) observed site amplification around 1 Hz at a station located near PDN. It is also mentioned that individual spectral ratios at the same station may vary considerably. Similarly, Imposa (2021) reports f_0 values between 1 and 2 Hz at the north east section of Etna (740 m a.s.l.) which were obtained by processing local earthquakes. The author attributes the large variations of the HVSR peak frequencies to the complexity of the seismic signal due to path taken by the wavefront in relation to the present volcano-tectonic structures.

Generally, the present three dimensional volcano-tectonic structures pose a source of error for the derivation of H/V peak frequencies. The scattering on interfaces affects the horizontal and vertical component of the wavefield differently and therefore influences the HVSR curve and subsequently the estimation of the H/V peak frequency.

7.1.1. Combined seismometer and DAS HVSRs

Although not consistent for all the fault-cable crossings, in general higher $A_{H/V}$ coincides with the presence of fault zones crossed by the cable. The pattern of elevated amplitude values along the cable is virtually identical to the residuals of the strain derivation using a volcanic explosion event in Currenti et al. (2021). It can be concluded that the maximum H/V amplitude is a good indicator for the high resolution detection of faults at the site. Thereby, the elevated values on the eastern loop of the fibre can then be interpreted as the NW-SE running fault extending further to the south.

The combined DAS and broadband spectral ratio can serve as a complement to the conventional site characterization when additional DAS data is available. Further investigation is necessary to illuminte the underlying mechanism, limitations, spatial stability and possible influence of the fault geometry on the result.

7.1.2. Geological interpretation

Geological descriptions and maps, e.g. by Azzaro et al. (2012), Branca (2011) or Pichler (1984), consistently describe the PDC area as delimited by the exposed rim of the old Ellittico caldera from the north to the southeast with the rim dipping down towards the center of the array layout.

SESAME (2004) describes the influence of laterally varying structures on the shape of the H/V peak as inferred from numerical simulations. The authors associate ”sharp” or ”clear” peaks with a smooth subsurface topography i.e., ”gentle interface slopes”. Contrary, broader and generally lower peaks indicate a ”rapidly varying” layer thickness ”for instance at valley edges”. The interpretation of the corresponding area with the highest f_0 as the Ellittico caldera rim would therefore be consistent with the geological information and explain the shape of the HVSR curves in question. The transition to the area where the caldera rim is imaged is delimited by the already mapped fault at the center and the suggested extension of the NE-SW trending fault further to the south. Secondary peaks in the northern part of the array could hint to additional shallow strong resonators e.g., lava flows (Coltelli et al., 1994).

7.1.3. Comparison with magnetic survey Napoli et al. (2021)

Napoli et al. (2021) provides a high resolution magnetic survey of the PDC area. The derived main subsurface structures are largely in agreement with the ones indicated by the interpolated f_0-map.

The areas with higher f_0 in the northeast and at the eastern border of the array coincide with the displayed magnetic anomalies (figure F.1) and in both results the structure is delimited by the fault crossing NNW-SSE. Smaller anomalies west of this fault zone are consistent with moderately high peak frequencies ($\approx$ 1) Hz on stations BB25, BB26, BB21 and BB17.

The elevated f_0 of 1.17 Hz on BB06 at the southeastern edge corresponds to a strong negative anomaly, marking the transition to a different system of lava flows (Branca, 2011).

The modelled profile BB' in Napoli et al. (2021) (figure F.2) indicates a possible and previously not mapped fault east of the center fault zone. This would be conforming with the proposed progression of the eastern fault to the south of the site.

7.2. SPAC and 1D velocity model

The obtained SPAC curves largely follow the expected behaviour. The frequency band in which the curves exhibt Bessel-like shapes is determined by two factors. The upper frequency limit is given by the minimum resolvable wavelength, i.e., the minimum interstation distance of the array. This explains why the significant bandwidth shifts towards lower frequencies for rings with larger radii. The lower frequency limit is given by the drastic decrease of energy in the wavefield below ≈ 0.8 - 1 Hz.

Additionally, the presence of uncorrelated noise, the very limited azimuthal uniform distribution of tremor sources and the aforementioned 3D effects are possible factors that might influence the shape of the curves towards a non-ideal Bessel function. Nonetheless, the curves for smaller rings are in good agreement with the chosen reference model which indicates a similar velocity distribution in the shallower area. In the first inversion result, it can be seen that both models show very low v_S values in the upper part.

The inversion of the SPAC curves produces a model under the assumption that the subsurface velocity distribution is completely one dimensional, i.e. there are no lateral variations. This is because the inversion returns an averaged model of the subsurface under the complete array (Wathelet et al., 2004). As was demonstrated, the assumption of lateral homogeneity does not hold for the investigated site. Resulting models should therefore be interpreted accordingly.

As was discussed in section 5.3, the v_P profile has only very limited influence on the shape of the SPAC curve. This is reflected in the parameter space, where the v_P parameters show no convergence and no relation between parameter value and model misfit is noteable. All the v_S parameters and $d_{S,0}$ are converging towards a unique value, indicating a stable solution. However, $d_{S,1}$ is less well resolved. This is illustrated by the 50 models with the lowest misfit (figure 7.1). While most models indeed show the bottom depth of the second layer around 65 m there is a variation of around 8 m.

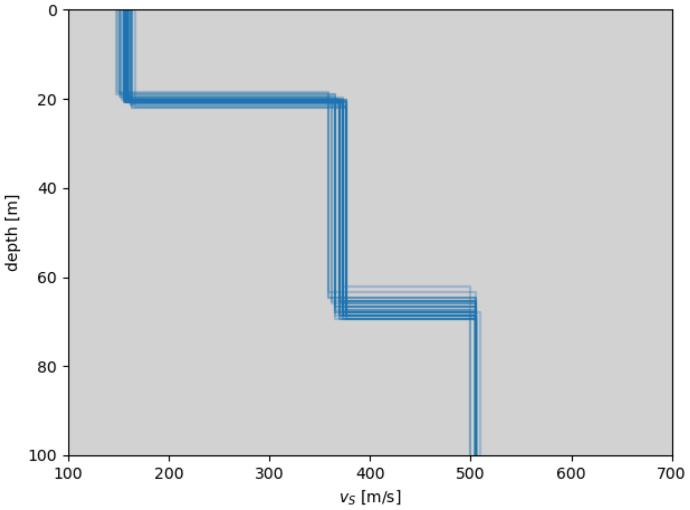

Figure 7.1.: The 50 v_S models with lowest misfit, obtained by inversion of SPAC curves

The study of Wegler and Seidl (1997) provides a 1D velocity model of PDC obtained as well by the spatial autocorrelation method. Only three stations were used and a limited bandwidth could be investigated which results in low resolution in the top layers. According to Scherbaum et al. (2003) an impedance contrast can be overestimated due to a too simple parametrization. As the model is only constituted by a single layer over half-space, the absolute velocity values of the half-space should be treated with caution. Punzo et al. (2011) present a three layer velocity model, the result of active source seismics on the north east flank of Etna. All three models agree on the low v_S of roughly 130 $\frac{m}{s}$ in the top layer. The interface of the obtained model lies only slightly shallower than the transition to half-space in both Wegler and Seidl (1997) and Punzo et al. (2011). Both reference model's last bottom depth is at around 25 m, constituting a strong velocity increase to approximately 700 $\frac{m}{s}$ in the half-space. Contrary, the v_S model of this study shows two intermediate contrasts, with the second at 65 m and a bottom velocity of just over 500 $\frac{m}{s}$. The discrepancy is probably the result of the spatial averaging nature of SPAC and the lateral heterogeneities of PDC. This can be further illustrated by applying equation 2.3 with the average v_S of the two upper layers of $\approx$ 270 $\frac{m}{s}$ and a depth of 65 m. This gives a fundamental frequency of 1.04 Hz which is close to the obtained mean fundamental frequency of 1.00 Hz.

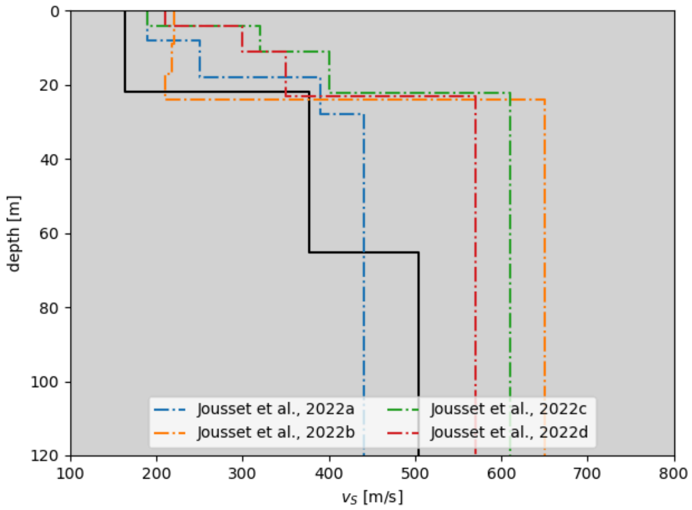

Figure 7.2.: v_S model with lowest misfit, obtained by inversion of SPAC curves, together with models from Jousset et al. (2022)

Figure 7.2 shows the comparison with the four v_S models of Jousset et al. (2022). These were obtained by multichannel analysis of surface waves on the northwestern and southwestern parts of the co-located DAS layout. All four models show slightly higher $v_{S,0}$ values and models b to d agree in an abrupt transition to half-space with a v_S of 560 to 650 $\frac{m}{s}$ at around 24 m. This depth is consistent with the inferred velocity contrast at 22 m, while the second interface at 64 m is not in agreement with Jousset et al. (2022). However, the difference in the half-space velocity is not as large as for the proposed models of Wegler and Seidl (1997) and Punzo et al. (2011). Additionally the resolution of the method used in Jousset et al. (2022) is presumably limited to depths < 50 m. Zuccarello et al. (2016) conducted a study at the northeast sector of Etna based on the processing of seismic noise. They found velocities of around 150 $\frac{m}{s}$ in the uppermost layers and an abrupt velocity increase to 600 $\frac{m}{s}$ at about 60 m from from inversion of DCs and HVSR curves. Closer to the crater area, Del Pezzo et al. (1993) report velocities of < 200 $\frac{m}{s}$ in the 1 to 2 Hz band of the volcanic tremor. Thus, both studies are generally in agreement with the model obtained here.

7.3. Joint inversion

The solutions to the joint inversion problem, show the expected behaviour when adding the different H/V peaks to the inversion scheme. The bottom depth of the second layer increases when including the lower peak frequency and decreases when including the higher f_0. When inverting the SPAC curves only, the solution represents the average between both cases.

Although the misfit could be reduced significantly, both models still depict an average of the subsurface velocity distribution, especially for the northeastern area of PDC. For more precise velocity models, one or several smaller and more dense arrays would be appropriate. This way, the assumption of an approximately one-dimensional velocity distribution within the array would hold true. Smaller station spacing would extend the usable frequency range so that the full tremor wavefield could be analyzed. Thus, a better fit of the Bessel functions can be achieved as the computed SPAC coefficients should ideally span at least the first arc of the function (Chouet, 1996).

7.4. Implications for resonator depth

The depth of the first subsurface impedance contrast in the survey area can be estimated by using equation 2.3 as

$$d = \frac{v_{S,0}}{4f_0}$$

For $v_{S,0}$ the averaged velocity of the two upper layers in both models described in 6.4 are assumed, i.e. 253 and 249 $\frac{m}{s}$, respectively. With $f_0 = 1.19$ Hz, this yields a resonator depth of 53 m in the northeastern sector of the site. For the remaining stations and f_0 of 0.91 Hz, a depth of 68 m results. When the layer's velocities are weighted by their respective thickness before averaging, these depth values change to 58 and 78 m. These estimations correspond to the transition to half-space of the inferred velocity models from joint inversion.

Inserting $v_{S,0} = 170$ $\frac{m}{s}$ and the secondary H/V peaks of 5 to 6 Hz, this indicates a second strong contrast at 7 to 8.5 m depth below the corresponding stations. This can also be seen in the solution models c and d in Jousset et al. (2022). Additionally all depth estimates are consistent with the study of Coltelli et al. (1994) and their assessment of both the PDC and PDN geological units.

8. Conclusion

This work attempted to obtain a site characterization of the Piano delle Concazze area at the northeast flank of Etna.

Using horizontal-to-vertical spectral ratios the main geological subsurface structures have been mapped. The result is consistent with published geological and magnetic survey information. Extending the method to a combined DAS and broadband H/V ratio allowed to confirm existing fault structures. Additionally, previously unmapped faults could be illuminated and are in agreement with the suggestions of independent studies.

This way, the potential of DAS to complement conventional methods for site characterization was demonstrated. Strain-rate data can easily be incorporated using a simple approach and minimal changes to the program and only using noise data. In subsequent studies, the peak frequency of the combined HVSR needs to be adressed, as well as the influence fault geometry has on its amplitude. The transformation of strain-rate records to velocity records could improve the results.

Moreover, it was found that volcanic activity heavily influences the spectral ratios. A detailed study on this behaviour could investigate if the change in H/V ratio can be related to specific volcanic processes or tremor source regions.

An average 1D shear wave velocity model was derived using the spatial autocorrelation method. By jointly inverting the autocorrelation curves and HVSR peak frequencies, two additional models for the northeastern area and the rest of the investigation site were obtained. The models are valuable as a reference for further studies, especially using the fibre optic cable. They can also serve as starting models for more sophisticated imaging methods. The inferred 1D velocity distributions are generally in agreement with available models from the site and the general area. They are however subject to the influence of lateral subsurface heterogeneities.

To improve the outcome further, smaller and denser array configurations would be necessary in order to extend the resolvable frequency range and meet the assumption of lateral homogeneity.

Acknowledgements

I would like to thank both of my supervisors, Philippe and Matthias, for their continued support, advice and patience not only during the time of this thesis, but over the last years.

I am very grateful to everyone else who helped me in one way or the other, be it scientific, personal or both: Michael Weber, Gilda Currenti, Charlotte Krawczyk, Martina Rosskopf, Sergio Diaz, Henry Harms and Gurur Beydağ. Thank you for your professional help and advice, for material and data, for proofreading, encouragement and friendship.

A special *Danke* to my parents for their everlasting trust and support and who made all of this possible.

Selbstständigkeitserklärung

Hiermit versichere ich, dass ich die vorliegende Arbeit ohne Hilfe Dritter und ohne Zuhilfenahme anderer als der angegebenen Quellen und Hilfsmittel angefertigt habe. Die den benutzten Quellen wörtlich oder inhaltlich entnommenen Stellen sind als solche kenntlich gemacht. Die „Richtlinie zur Sicherung guter wissenschaftlicher Praxis für Studierende an der Universität Potsdam (Plagiatsrichtlinie) - Vom 20. Oktober 2010“ habe ich zur Kenntnis genommen.

Ort und Datum

Unterschrift

Bibliography

Aki, K. (1957). Space and Time Spectra of Stationary Stochastic Waves, with Special Reference to Microtremors. *Bulletin of the Earthquake Research Institute*, *35*.

Aki, K. (1965). A note on the use of microseisms in determining the shallow structure of the Earth's crust. *Geophysics*, *30*(4), 665–666. https://doi.org/10.1190/1.1439640

Albarello, D., & Lunedei, E. (2013). Combining horizontal ambient vibration components for H/V spectral ratio estimates. *Geophysical Journal International*, *194*(2), 936–951. https://doi.org/10.1093/gji/ggt130

Azzaro, R., Branca, S., Gwinner, K., & Coltelli, M. (2012). The volcano-tectonic map of Etna volcano, 1:100.000 scale: an integrated approach based on a morphotectonic analysis from high-resolution DEM constrained by geologic, active faulting and seismotectonic data. *Italian Journal of Geosciences*, *131*(1), 153–170. https://doi.org/10.3301/IJG.2011.29

Behncke, B., Branca, S., Corsaro, R. A., De Beni, E., Miraglia, L., & Proietti, C. (2014). The 2011–2012 summit activity of Mount Etna: Birth, growth and products of the new SE crater. *Journal of Volcanology and Geothermal Research*, *270*, 10–21. https://doi.org/10.1016/j.jvolgeores.2013.11.012

Bettig, B., Bard, P., Scherbaum, F., Riepl, J., Cotton, F., Cornou, C., & Hatzfeld, D. (2001). Analysis of dense array noise measurements using the modified spatial auto-correlation method (SPAC): application to the Grenoble area. *Bollettino Di Geofisica Teorica Ed Applicata*, *42*, 281–304.

Bisson, M., Spinetti, C., Andronico, D., Palaseanu-Lovejoy, M., Fabrizia Buongiorno, M., Alexandrov, O., & Cecere, T. (2021). Ten years of volcanic activity at Mt Etna: High-resolution mapping and accurate quantification of the morphological changes by Pleiades and Lidar data. *International Journal of Applied Earth Observation and Geoinformation*, *102*. https://doi.org/10.1016/j.jag.2021.102369

Bonaccorso, A., Calvari, S., Coltelli, M., Negro, C., & Falsaperla, S. (2004). *Mt. Etna: Volcano laboratory* (Vol. 143).

Bonnefoy-Claudet, S., Cotton, F., & Bard, P.-Y. (2006). The nature of noise wavefield and its applications for site effects studies: A literature review. *Earth-Science Reviews*, *79*(3), 205–227. https://doi.org/0.1016/j.earscirev.2006.07.004

Bonnefoy-Claudet, S., Köhler, A., Cornou, C., Wathelet, M., & Bard, P.-Y. (2008). Effects of Love Waves on Microtremor H/V Ratio. *Bulletin of the Seismological Society of America*, *98*, 288–300. https://doi.org/10.1785/0120070063

Branca, S. (2011). Geological map of Etna volcano. 1:50.000 scale. *Italian Journal of Geosciences*, *130*(3), 265–291. https://doi.org/10.3301/ijg.2011.15

Branca, S., Coltelli, M., & Groppelli, G. (2011). Geological evolution of a complex basaltic stratovolcano: Mount Etna, Italy. *Italian Journal of Geosciences*, (Vol. 130, n. 3), 306–317. https://doi.org/10.3301/ijg.2011.13

Cannata, A., Di Grazia, G., Aliotta, M., Cassisi, C., Montalto, P., & Patanè, D. (2013). Monitoring Seismo-volcanic and Infrasonic Signals at Volcanoes: Mt. Etna Case Study. *Pure and Applied Geophysics*, *170*. https://doi.org/10.1007/s00024-012-0634-x

Chester, D. K. (1985). *Mount Etna : the anatomy of a volcano*. Chapman; Hall.

Cho, I. (2022). Spatial autocorrelation method for simple microtremor array survey at rock/stiff-soil sites. *Geophysical Journal International*, *233*(2), 1296–1317. https://doi.org/10.1093/gji/ggac522

Chouet, B. A. (1996). New methods and future trends in seismological volcano monitoring. In *Monitoring and mitigation of volcano hazards* (pp. 23–97). Springer Berlin Heidelberg. https://doi.org/10.1007/978-3-642-80087-0_2

Chouet, B. A. (2003). Volcano Seismology. *Pure and Applied Geophysics*, *160*(3), 739–788. https://doi.org/10.1007/pl00012556

Chouet, B. A., & Matoza, R. S. (2013). A multi-decadal view of seismic methods for detecting precursors of magma movement and eruption. *Journal of Volcanology and Geothermal Research*, *252*, 108–175. https://doi.org/10.1016/j.jvolgeores.2012.11.013

Coltelli, M., Garduno, V., Neri, M., Pasquarè, G., & Pompilio, M. (1994). Geology of the northern wall of the Valle del Bove, Mt. Etna (Sicily). *Acta Vulcanologica*, (5), 55–68.

Currenti, G., Jousset, P., Napoli, R., Krawczyk, C., & Weber, M. (2021). On the comparison of strain measurements from fibre optics with a dense seismometer array at Etna volcano (Italy). *Solid Earth*, *12*(4), 993–1003. https://doi.org/10.5194/se-12-993-2021

Del Pezzo, E., De Martino, S., Gresta, S., Martini, M., Milana, G., Patanè, D., & Sabbarese, C. (1993). Velocity and spectral characteristics of the volcanic tremor at Etna deduced by a small seismometer array. *Journal of Volcanology and Geothermal Research*, *56*(4), 369–378. https://doi.org/10.1016/0377-0273(93)90003-A

Di Giulio, G., Cara, F., Rovelli, A., Lombardo, G., & Rigano, R. (2009). Evidences for strong directional resonances in intensely deformed zones of the Pernicana fault, Mount Etna, Italy. *Journal of Geophysical Research*, *114*(B10). https://doi.org/10.1029/2009jb006393

Di Grazia, G., Falsaperla, S., & Langer, H. (2006). Volcanic tremor location during the 2004 Mount Etna lava effusion. *Geophysical Research Letters*, *33*(4). https://doi.org/10.1029/2005gl025177

Diaz-Meza, S., Jousset, P., Currenti, G., Wollin, C., Krawczyk, C., Clarke, A., & Chalari, A. (2023). On the Comparison of Records from Standard and Engineered Fiber Optic Cables at Etna Volcano (Italy). *Sensors*, *23*(7). https://doi.org/10.3390/s23073735

Díaz-Moreno, A., Barberi, G., Cocina, O., Koulakov, I., Scarfì, L., Zuccarello, L., Prudencio, J., García-Yeguas, A., Álvarez, I., García, L., & Ibáñiez, J. M. (2017). New Insights on Mt. Etna's Crust and Relationship with the Regional Tectonic Framework from Joint Active and Passive P-Wave Seismic Tomography. *Surveys in Geophysics*, *39*(1), 57–97. https://doi.org/10.1007/s10712-017-9425-3

Doglioni, C., Innocenti, F., & Mariotti, G. (2001). Why Mt Etna? *Terra Nova*, *13*(1), 25–31. https://doi.org/10.1046/j.1365-3121.2001.00301.x

Eibl, E. P. S., Rosskopf, M., Sciotto, M., Currenti, G., Di Grazia, G., Jousset, P., Krüger, F., & Weber, M. (2022). Performance of a Rotational Sensor to Decipher Volcano Seismic Signals on Etna, Italy. *Journal of Geophysical Research: Solid Earth*, *127*(6). https://doi.org/10.1029/2021JB023617

Flores Estrella, H., & González, J. (2002). SPAC: An alternative method to estimate earthquake site effects in Mexico City. *Geofísica Internacional*, *42*. https://doi.org/10.22201/igeof.00167169p.2003.42.2.267

Foti, S., Hollender, F., Garofalo, F., Albarello, D., Asten, M., Bard, P.-Y., Comina, C., Cornou, C., Cox, B., Giulio, G. D., Forbriger, T., Hayashi, K., Lunedei, E., Martin, A., Mercerat, D., Ohrnberger, M., Poggi, V., Renalier, F., Sicilia, D., & Socco, V. (2017). Guidelines for the good practice of surface wave analysis. *Bulletin of earthquake engineering*, *16*(6), 2367–2420. https://doi.org/10.1007/s10518-017-0206-7

Giuffrida, M., Scandura, M., Costa, G., Zuccarello, F., Sciotto, M., Cannata, A., & Viccaro, M. (2021). Tracking the summit activity of Mt. Etna volcano between July 2019 and January 2020 by integrating petrological and geophysical data. *Journal of Volcanology and Geothermal Research*, *418*, 107350. https://doi.org/10.1016/j.jvolgeores.2021.107350

Haney, M., Mikesell, T., van Wijk, K., & Nakahara, H. (2012). Extension of the spatial autocorrelation (SPAC) method to mixed-component correlations of surface waves. *Geophysical Journal International*, *191*(1), 189–206. https://doi.org/10.1111/j.1365-246X.2012.05597.x

Hobiger, M., Hallo, M., Schmelzbach, C., Stähler, S., Fäh, D., Giardini, D., Golombek, M., Clinton, J., Dahmen, N., Zenhäusern, G., Knapmeyer-Endrun, B., Carrasco Morales, S., Charalambous, C., Hurst, K., Kedar, S., & Banerdt, W. (2021). The shallow structure of Mars at the InSight landing site from inversion of ambient vibrations. *Nature Communications*, *12*, 6756. https://doi.org/10.1038/s41467-021-26957-7

Ikeda, T., Asten, M., & Matsuoka, T. (2013). Joint inversion of spatial autocorrelation curves with HVSR for site characterization in Newcastle, Australia. *ASEG Extended Abstracts*, *2013*, 1. https://doi.org/10.1071/ASEG2013ab315

Imposa, S. (2021). The role of the volcano-tectonic structure on the seismic site response: An application in the northeastern sector of Mt. Etna volcano, Sicily, Italy. *Contributions to Geophysics and Geodesy*, *37*(1), 59–70. https://journal.geo.sav.sk/cgg/article/view/291

INGV. (2019a). *ETNA Bollettino Settimanale 01/07/2019 - 07/07/2019* (tech. rep. No. 28). IGNV Catania.

INGV. (2019b). *ETNA Bollettino Settimanale 22/07/2019 - 28/07/2019* (tech. rep. No. 31). IGNV Catania.

INGV. (2019c). *ETNA Bollettino Settimanale 19/08/2019 - 25/08/2019* (tech. rep. No. 35). IGNV Catania.

INGV. (2019d). *ETNA Bollettino Settimanale 16/09/2019 - 22/09/2019* (tech. rep. No. 39). IGNV Catania.

Jousset, P., Currenti, G., Schwarz, B., Chalari, A., Tilmann, F., Reinsch, T., Zuccarello, L., Privitera, E., & Krawczyk, C. (2022). Fibre optic distributed acoustic sensing of volcanic events. *Nature Communications*, *13*(1753). https://doi.org/10.1038/s41467-022-29184-w

Kawakatsu, H., & Yamamoto, M. (2015). Volcano Seismology. In *Treatise on Geophysics* (pp. 389–419). Elsevier. https://doi.org/10.1016/b978-0-444-53802-4.00081-6

Köhler, A., Ohrnberger, M., Scherbaum, F., Wathelet, M., & Cornou, C. (2007). Assessing the reliability of the modified three-component spatial autocorrelation technique. *Geophysical Journal International*, *168*(2), 779–796. https://doi.org/10.1111/j.1365-246X.2006.03253.x

Konno, K., & Ohmachi, T. (1998). Ground-motion characteristics estimated from spectral ratio between horizontal and vertical components of microtremor. *Bulletin of the Seismological Society of America*, *88*(1), 228–241. https://doi.org/10.1785/BSSA0880010228

Konstantinou, K. I., & Schlindwein, V. (2003). Nature, wavefield properties and source mechanism of volcanic tremor: A review. *Journal of Volcanology and Geothermal Research*, *119*(1-4), 161–187. https://doi.org/10.1016/s0377-0273(02)00311-6

Lanza, F., Kenyon, L. M., & Waite, G. P. (2016). Near-Surface Velocity Structure of Pacaya Volcano, Guatemala, Derived from Small-Aperture Array Analysis of Seismic Tremor. *Bulletin of the Seismological Society of America*, *106*(4), 1438–1445. https://doi.org/10.1785/0120150275

Lermo, J., & Chávez-García, F. J. (1993). Site effect evaluation using spectral ratios with only one station. *Bulletin of the Seismological Society of America*, *83*(5), 1574–1594. https://doi.org/10.1785/BSSA0830051574

Li, F., Valero, M., Cheng, Y., & Song, W. (2019). High-Frequency Time-Lapse Seismic Spatial Autocorrelation Imaging Shallow Velocity Variations. *IEEE Journal of Selected Topics in Applied Earth Observations and Remote Sensing*, *12*(12), 5385–5390. https://doi.org/10.1109/JSTARS.2019.2954114

Lontsi, A. M., Sánchez-Sesma, F. J., Molina-Villegas, J. C., Ohrnberger, M., & Krüger, F. (2015). Full microtremor H/V(z, f) inversion for shallow subsurface characterization. *Geophysical Journal International*, *202*(1), 298–312. https://doi.org/10.1093/gji/ggv132

Maresca, R., Nardone, L., Galluzzo, D., La Rocca, M., & Del Pezzo, E. (2006). Application of the SPAC method to ambient noise recorded in the Vesuvius area (Italy).

McNutt, S. R. (2005). Volcanic Seismology. *Annual Review of Earth and Planetary Sciences*, *33*(1), 461–491. https://doi.org/10.1146/annurev.earth.33.092203.122459

Molnar, S., Cassidy, J., Castellaro, S., Cornou, C., Crow, H., Hunter, J., Matsushima, S., Sánchez-Sesma, F., & Yong, A. (2018). Application of Microtremor Horizontal-to-Vertical Spectral Ratio (MHVSR) Analysis for Site Characterization: State of the Art. *Surveys in Geophysics*, *39*(4), 613–631. https://doi.org/10.1007/s10712-018-9464-4

Molnar, S., Sirohey, A., Assaf, J., Bard, P.-Y., Castellaro, S., Cornou, C., Cox, B., Guillier, B., Hassani, B., Kawase, H., Matsushima, S., Sánchez-Sesma, F., & Yong, A. (2022). A review of the microtremor horizontal-to-vertical spectral ratio (MHVSR) method. *Journal of Seismology*, *26*, 1–33. https://doi.org/10.1007/s10950-021-10062-9

Mora, M. M., Lesage, P., Dorel, J., Bard, P.-Y., Métaxian, J.-P., Alvarado, G. E., & Leandro, C. (2001). Study of seismic site effects using H/V spectral ratios at Arenal Volcano, Costa Rica. *Geophysical Research Letters*, *28*(15), 2991–2994. https://doi.org/https://doi.org/10.1029/2001GL013049

Mora, M. M., Lesage, P., Valette, B., Alvarado, G. E., Leandro, C., Métaxian, J.-P., & Dorel, J. (2006). Shallow velocity structure and seismic site effects at Arenal volcano, Costa Rica. *Journal of*

Volcanology and Geothermal Research, *152*(1), 121–139. https://doi.org/10.1016/j.jvolgeores.2005.09.013

Mucciarelli, M., & Gallipoli, M. (2001). A critical review of 10 years of microtremor HVSR technique. *Bollettino di Geofisica Teorica ed Applicata*, *42*, 255–266.

Nakahara, H. (2012). Formulation of the spatial autocorrelation (SPAC) method in dissipative media. *Geophysical Journal International*, *190*(3), 1777–1783. https://doi.org/10.1111/j.1365-246X.2012.05591.x

Nakahara, H., Emoto, K., & Nishimura, T. (2021). Extending the formulation of the spatial autocorrelation (SPAC) method to strain, rotation and tilt. *Geophysical Journal International*, *227*(1), 287–302. https://doi.org/10.1093/gji/ggab217

Nakamura, Y. (1989). A method for dynamic characteristics estimation of subsurface using microtremor on the ground surface. *Quarterly Report of Railway Technical Research Institute*, *30*.

Napoli, R., Currenti, G., & Sicali, A. (2021). Magnetic signatures of subsurface faults on the northern upper flank of Mt Etna (Italy). *Annals of Geophysics*, *64*. https://doi.org/10.4401/ag-8582

Nardone, L., & Maresca, R. (2011). Shallow Velocity Structure and Site Effects at Mt. Vesuvius, Italy, from HVSR and Array Measurements of Ambient Vibrations. *Bulletin of the Seismological Society of America*, *101*(4), 1465–1477. https://doi.org/10.1785/0120100165

Palaseanu-Lovejoy, M., Bisson, M., Spinetti, C., Buongiorno, M. F., Alexandrov, O., & Cecere, T. (2019). High-Resolution and Accurate Topography Reconstruction of Mount Etna from Pleiades Satellite Data. *Remote Sensing*, *11*(24). https://doi.org/10.3390/rs11242983

Panzera, F., Lombardo, G., Longo, E., Langer, H., Branca, S., Azzaro, R., Cicala, V., & Trimarchi, F. (2016). Exploratory seismic site response surveys in a complex geologic area: a case study from Mt. Etna volcano (southern Italy). *Natural Hazards*, *86*(S2), 385–399. https://doi.org/10.1007/s11069-016-2517-4

Parolai, S., & Galiana-Merino, J. J. (2006). Effect of Transient Seismic Noise on Estimates of h/v Spectral Ratios. *Bulletin of the Seismological Society of America*, *96*(1), 228–236. https://doi.org/10.1785/0120050084

Parolai, S., Picozzi, M., Richwalski, S. M., & Milkereit, C. (2005). Joint inversion of phase velocity dispersion and H/V ratio curves from seismic noise recordings using a genetic algorithm, considering higher modes. *Geophysical Research Letters*, *32*(1). https://doi.org/10.1029/2004gl021115

Patanè, D., Cocina, O., Falsaperla, S., Privitera, E., & Spampinato, S. (2004). Mt. Etna Volcano: A Seismological Framework. In *Mt. Etna: Volcano Laboratory* (pp. 147–165). https://doi.org/https://doi.org/10.1029/143GM10

Patanè, D., Ferrucci, F., & Gresta, S. (1994). Spectral features of microearthquakes in volcanic areas: Attenuation in the crust and amplitude response of the site at Mt. Etna, Italy. *Bulletin of the Seismological Society of America*, *84*(6), 1842–1860. https://doi.org/10.1785/BSSA0840061842

Perrier, L., Métaxian, J.-P., Battaglia, J., & Garaebiti, E. (2012). Estimation of the near-surface velocity structure of the Yasur-Yenkahe volcanic complex, Vanuatu. *Journal of Volcanology and Geothermal Research*, *227-228*, 50–60. https://doi.org/10.1016/j.jvolgeores.2011.12.006

Pichler, H. (1984). *Italienische Vulkangebiete IV.* Schweizerbart Science Publishers. http://www.schweizerbart.de//publications/detail/isbn/9783443150372/Bd%5C_76%5C_Sammlung%5C_Geol%5C_Fuhrer%5C_Ital%5C_Vulka

Pilz, M., & Parolai, S. (2012). Tapering of windowed time series. *New Manual of Seismological Observatory Practice 2 (NMSOP2).* https://doi.org/10.2312/GFZ.NMSOP-2_IS_14.1

Punzo, M., Varriale, F., Bruno, P., Rovelli, A., & Di Giulio, G. (2011). *Esperimento di sismica attiva in onde S con sorgente vibratoria Ivi-MiniVib in corrispondenza della faglia della Pernicana nel comune di Linguaglossa (CT)* (tech. rep.). AMRA S.C.Ar.l.

Renalier, F., Jongmans, D., Sawaidis, A., Wathelet, M., Knapmeyer-Endrun, B., & Cornou, C. (2010). Influence of parameterization on inversion of surface wave dispersion curves and definition of an inversion strategy for sites with a strong V-S contrast. *Geophysics*, *75*. https://doi.org/10.1190/1.3506556

Saccorotti, G., Maresca, R., & Del Pezzo, E. (2001). Array analyses of seismic noise at Mt. Vesuvius Volcano, Italy. *Journal of Volcanology and Geothermal Research*, *110*(1), 79–100. https://doi.org/10.1016/S0377-0273(01)00204-9

Saccorotti, G., Zuccarello, L., Pezzo, E. D., Ibanez, J., & Gresta, S. (2004). Quantitative analysis of the tremor wavefield at Etna Volcano, Italy. *Journal of Volcanology and Geothermal Research*, *136*(3-4), 223–245. https://doi.org/10.1016/j.jvolgeores.2004.04.003

Sambridge, M. (1999). Geophysical inversion with a neighbourhood algorithm—I. Searching a parameter space. *Geophysical Journal International*, *138*(2), 479–494. https://doi.org/10.1046/j.1365-246X.1999.00876.x

Sánchez-Sesma, F. J., Rodríguez, M., Iturrarán-Viveros, U., Luzón, F., Campillo, M., Margerin, L., García-Jerez, A., Suarez, M., Santoyo, M. A., & Rodríguez-Castellanos, A. (2011). A theory for microtremor H/V spectral ratio: application for a layered medium. *Geophysical Journal International*, *186*(1), 221–225. https://doi.org/10.1111/j.1365-246X.2011.05064.x

Scherbaum, F., Hinzen, K.-G., & Ohrnberger, M. (2003). Determination of shallow shear wave velocity profiles in the Cologne, Germany area using ambient vibrations. *Geophysical Journal International*, *152*(3), 597–612. https://doi.org/10.1046/j.1365-246X.2003.01856.x

Sciotto, M., Cannata, A., Di Grazia, G., & Montalto, P. (2022). Volcanic tremor and long period events at Mt. Etna: Same mechanism at different rates or not? *Physics of the Earth and Planetary Interiors*, *324*, 106850. https://doi.org/10.1016/j.pepi.2022.106850

SESAME. (2004). *Guidelines for the Implementation of the H/V Spectral Ratio Technique on Ambient Vibrations: Measurements, Processing and Interpretation.* SESAME European research project WP12.

Spica, Z., Perton, M., Martin, E. R., Beroza, G. C., & Biondi, B. (2020). Urban Seismic Site Characterization by Fiber-Optic Seismology. *Journal of Geophysical Research: Solid Earth*, *125*(3). https://doi.org/10.1029/2019jb018656

Spica, Z., Perton, M., Nakata, N., Liu, X., & Beroza, G. C. (2018). Shallow VS Imaging of the Groningen Area from Joint Inversion of Multimode Surface Waves and H/V Spectral Ratios. *Seismological Research Letters*, *89*(5), 1720–1729. https://doi.org/10.1785/0220180060

Srigutomo, W., Handayani, G., Pribadi, A., & Nugraha, A. (2018). Investigation of 1D shear wave velocity profile using the spatial autocorrelation (SPAC) method: Case study at West Park ITB Campus, Bandung, Indonesia. *ARPN Journal of Engineering and Applied Sciences*, *13*, 2096–2107.

Tsai, V. C., & Moschetti, M. P. (2010). An explicit relationship between time-domain noise correlation and spatial autocorrelation (SPAC) results. *Geophysical Journal International.* https://doi.org/10.1111/j.1365-246x.2010.04633.x

Vidal-Villegas, J. A., Huerta-López, C. I., Ramírez, E. E., Arce-Villa, R., & Vega-Guzmán, F. d. J. (2021). Experimental Approach on the Study of Ground-Motion Amplification at the Cerro Prieto Volcano, Mexicali Valley, Baja California, Mexico. *Seismological Research Letters*, *93*(2A), 798–813. https://doi.org/10.1785/0220200370

Villaseñor, A., Benz, H. M., Filippi, L., Luca, G. D., Scarpa, R., Patanè, G., & Vinciguerra, S. (1998). Three-dimensional P-wave velocity structure of Mt. Etna, Italy. *Geophysical Research Letters*, *25*(11), 1975–1978. https://doi.org/10.1029/98gl01240

Wassermann, J. (2009). Volcano Seismology. In P. Bormann (Ed.). Deutsches GeoForschungsZentrum GFZ. https://doi.org/10.2312/GFZ.NMSOP_r1_ch13

Wathelet, M. (2005). *Array recordings of ambient vibrations: surface-wave inversion* (Doctoral dissertation). Université de Liège.

Wathelet, M. (2008). An improved neighborhood algorithm: Parameter conditions and dynamic scaling. *Geophysical Research Letters*, *35*(9). https://doi.org/10.1029/2008GL033256

Wathelet, M., Jongmans, D., & Ohrnberger, M. (2004). Surface-wave inversion using a direct search algorithm and its application to ambient vibration measurements. *Near Surface Geophysics*, *2*(4), 211–221. https://doi.org/10.3997/1873-0604.2004018

Wathelet, M., Chatelain, J.-L., Cornou, C., Di Giulio, G., Guillier, B., Ohrnberger, M., & Savvaidis, A. (2020). Geopsy: A user-friendly open-source tool set for ambient vibration processing. *Seismological Research Letters*, *91*. https://doi.org/10.1785/0220190360

Wathelet, M., Jongmans, D., & Ohrnberger, M. (2005). Direct Inversion of Spatial Autocorrelation Curves with the Neighborhood Algorithm. *Bulletin of the Seismological Society of America*, *95*(5), 1787–1800. https://doi.org/10.1785/0120040220

Wegler, U., & Seidl, D. (1997). Kinematic parameters of the tremor wave field at Mt. Etna (Sicily). *Geophysical Research Letters*, *24*(7), 759–762. https://doi.org/10.1029/97GL00673

Xia, J., Miller, R., & Park, C. (1999). Estimation of near-surface shear-wave velocity by inversion of Rayleigh waves. *Geophysics*, *64*. https://doi.org/10.1190/1.1444578

Xu, R., & Wang, L. (2021). The horizontal-to-vertical spectral ratio and its applications. *EURASIP Journal on Advances in Signal Processing*, *2021*. https://doi.org/10.1186/s13634-021-00765-z

Zuccarello, L., Paratore, M., Rocca, M. L., Ferrari, F. D., Messina, A., Branca, S., Contrafatto, D., Galluzzo, D., & Rapisarda, S. (2016). Shallow velocity model in the area of Pozzo Pitarrone, Mt. Etna, from single station, array methods and borehole data. *Annals of Geophysics*, *59*, 0433. https://doi.org/10.4401/ag-7086

Appendices

A. Instrumentation details

Station ID	**Longitude** [°]	**Latitude** [°]	**Altitude** [m]	**Logger Manuf.**	**Logger Model**	**Logger Serial**	**Sensor Manuf.**	**Sensor Model**	**Sampling Rate [Hz]**	**Gain**
BB01	15.01448	37.76542	2797	DiGOS	DATA-CUBE^3	728	Nanometrics	Trillium Compact 120	200	4
BB02	15.01365	37.76519	2796	DiGOS	DATA-CUBE^3	729	Nanometrics	Trillium Compact 120	200	4
BB03	15.01269	37.76492	2797	DiGOS	DATA-CUBE^3	730	Nanometrics	Trillium Compact 120	200	4
BB04	15.01193	37.76467	2802	DiGOS	DATA-CUBE^3	731	Nanometrics	Trillium Compact 120	200	4
BB05	15.01124	37.76446	2803	DiGOS	DATA-CUBE^3	733	Nanometrics	Trillium Compact 120	200	4
BB06	15.01023	37.76415	2809	DiGOS	DATA-CUBE^3	734	Nanometrics	Trillium Compact 120	200	4
BB07	15.01075	37.76492	2806	DiGOS	DATA-CUBE^3	735	Nanometrics	Trillium Compact 120	200	4
BB08	15.01145	37.76513	2801	DiGOS	DATA-CUBE^3	736	Nanometrics	Trillium Compact 120	200	4
BB09	15.01224	37.76528	2798	DiGOS	DATA-CUBE^3	737	Nanometrics	Trillium Compact 120	200	4
BB10	15.01315	37.76556	2795	DiGOS	DATA-CUBE^3	738	Nanometrics	Trillium Compact 120	200	4
BB11	15.01401	37.76576	2796	DiGOS	DATA-CUBE^3	739	Nanometrics	Trillium Compact 120	200	4
BB12	15.01474	37.76601	2795	DiGOS	DATA-CUBE^3	759	Nanometrics	Trillium Compact 120	200	4
BB13	15.01475	37.76681	2797	DiGOS	DATA-CUBE^3	760	Nanometrics	Trillium Compact 120	200	4

Station ID	Longitude [°]	Latitude [°]	Altitude $[m]$	Logger Manuf.	Logger Model	Logger Serial	Sensor Manuf.	Sensor Model	Sampling Rate [Hz]	Gain
BB14	15.01433	37.76641	2798	DiGOS	DATA-CUBE^3	761	Nanometrics	Trillium Compact 120 0	200	4
BB15	15.01370	37.76636	2799	DiGOS	DATA-CUBE^3	763	Nanometrics	Trillium Compact 120	200	4
BB16	15.01322	37.76617	2802	DiGOS	DATA-CUBE^3	429	Nanometrics	Trillium Compact 120	200	4
BB17	15.01255	37.76596	2801	DiGOS	DATA-CUBE^3	430	Nanometrics	Trillium Compact 120	200	4
BB18	15.01172	37.76572	2803	DiGOS	DATA-CUBE^3	431	Nanometrics	Trillium Compact 120	200	4
BB19	15.01097	37.76555	2806	DiGOS	DATA-CUBE^3	432	Nanometrics	Trillium Compact 120	200	4
BB20	15.01123	37.76616	2806	DiGOS	DATA-CUBE^3	433	Nanometrics	Trillium Compact 120	200	4
BB21	15.01199	37.76638	2805	DiGOS	DATA-CUBE^3	434	Nanometrics	Trillium Compact 120	200	4
BB22	15.01282	37.76661	2804	DiGOS	DATA-CUBE^3	435	Nanometrics	Trillium Compact 120	200	4
BB23	15.01377	37.76689	2799	DiGOS	DATA-CUBE^3	436	Nanometrics	Trillium Compact 120	200	4
BB24	15.01315	37.76739	2800	DiGOS	DATA-CUBE^3	437	Nanometrics	Trillium Compact 120	200	4
BB25	15.01202	37.76715	2804	DiGOS	DATA-CUBE^3	438	Nanometrics	Trillium Compact 120	200	4
BB26	15.01148	37.76689	2807	DiGOS	DATA-CUBE^3	439	Nanometrics	Trillium Compact 120	200	4

B. Pizzi Deneri and Ellittico caldera rim

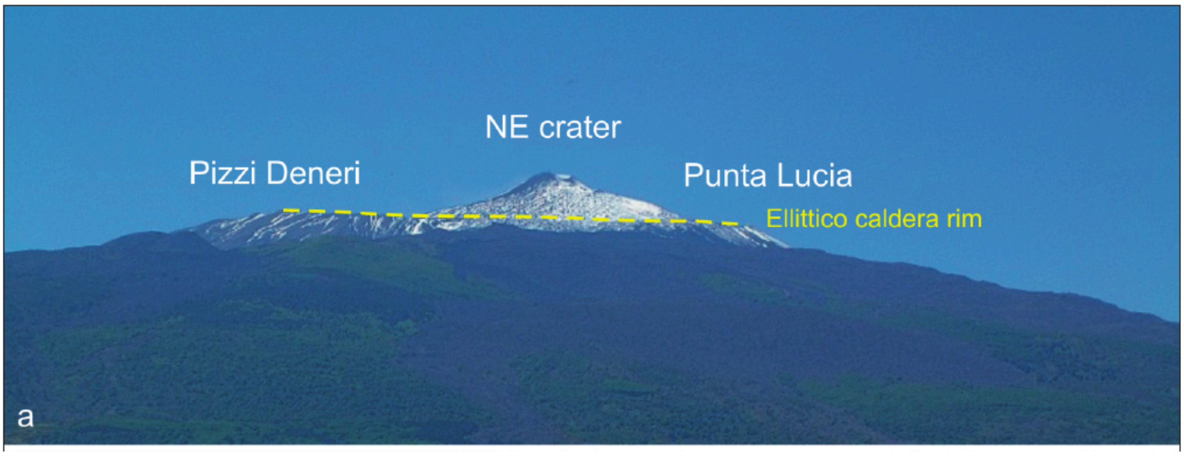

Figure B.1.: Northern flank of Etna with Ellittico caldera rim and location of Pizzi Deneri (from: Branca et al., 2011)

C. HVSRs August 30, 13h

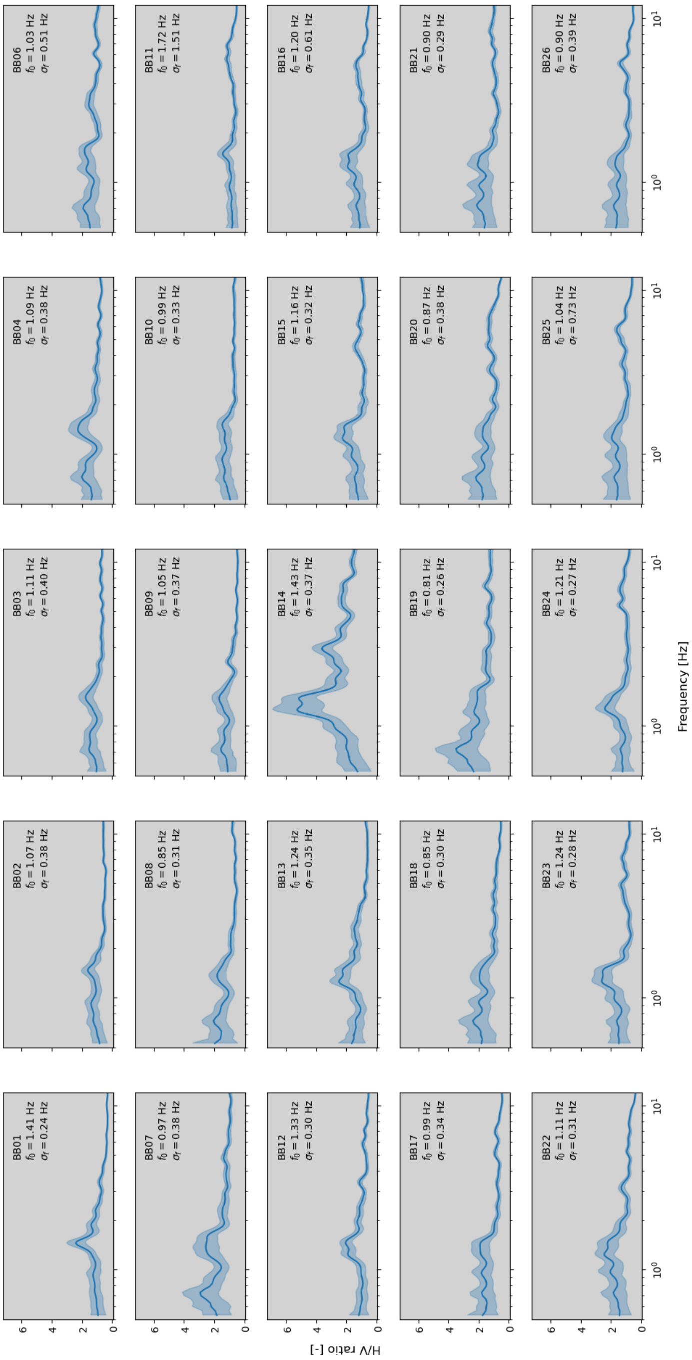

Figure C.1.: Example of unsuitable HVSRs from August 30, 13h; light blue area marks one standard deviation

D. Analysis of eruptive activity

D.1. July 27 to 29

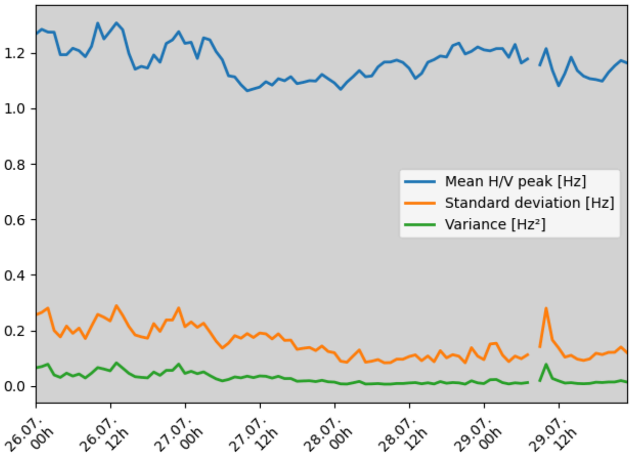

Figure D.1.: Mean H/V ratio over all stations with corresponding standard deviation and variance from July 26 to 29

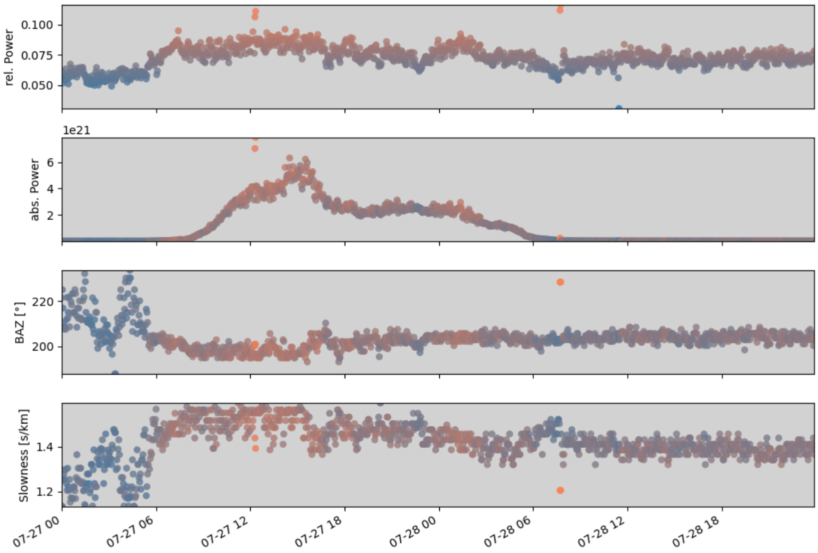

Figure D.2.: f-k analysis of the eruptive activity on September 27 and 28; window length = 300 s; colorscale corresponds to relative power; note the increase of absolute power coinciding with a stabilization of the BAZ values around 205°, pointing towards the active vent at the NSEC

D.2. September 8 to 12

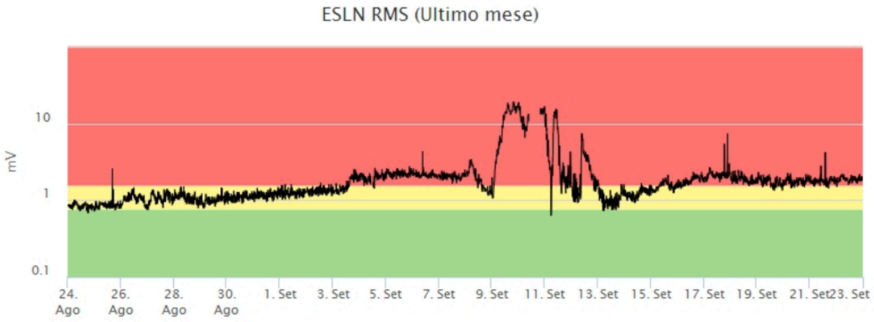

Figure D.3.: RMS tremor amplitude between August 24 and September 23 showing increased values from September 09 to 13 (from: INGV, 2019d)

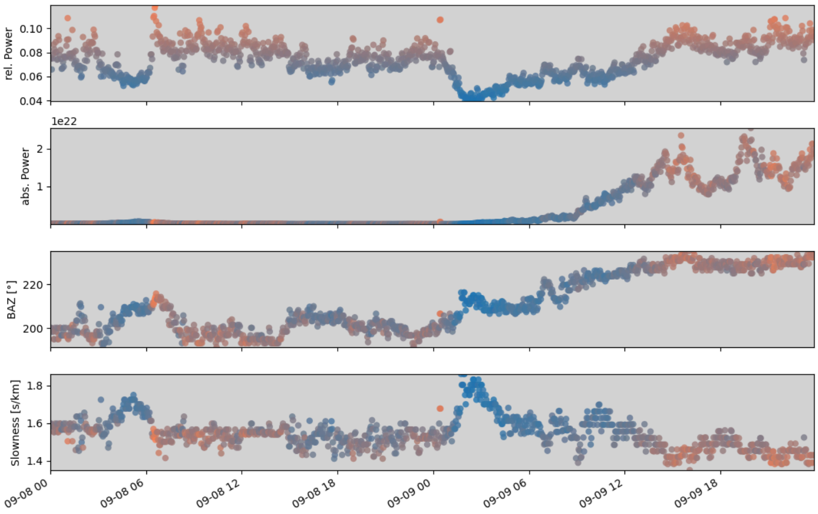

Figure D.4.: f-k analysis showing beginning of the eruptive activity on September 08 and 09; window length = 300 s; colorscale corresponds to relative power; note the increase of absolute power coinciding with a stabilization of the BAZ values around 230°, pointing towards the active vent at VOR

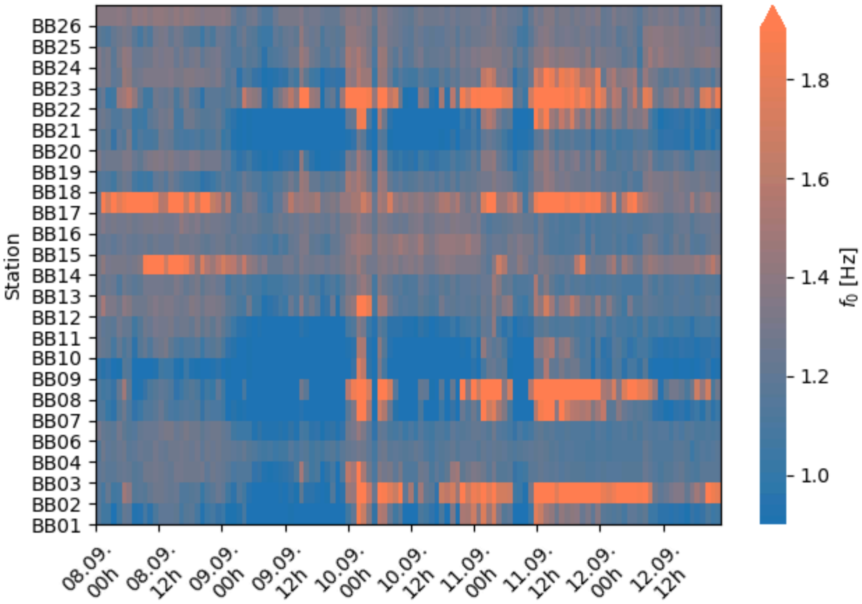

Figure D.5.: f_0 values averaged in one hour bins from September 08 to 12

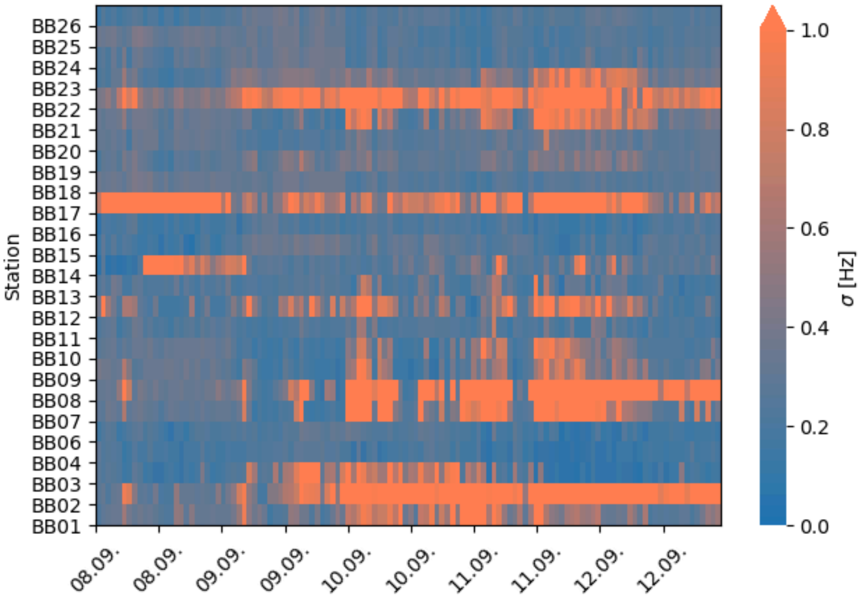

Figure D.6.: Corresponding σ values of the H/V peak frequencies in figure D.5

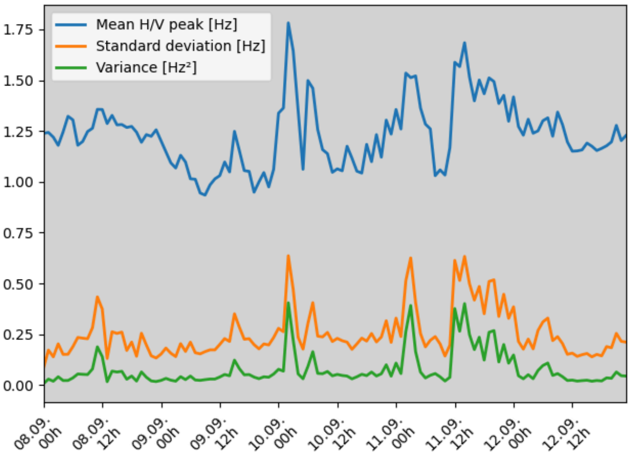

Figure D.7.: Mean H/V peak frequency over all stations with corresponding standard deviation and variance from September 08 to 12

E. Misfits of joint inversion

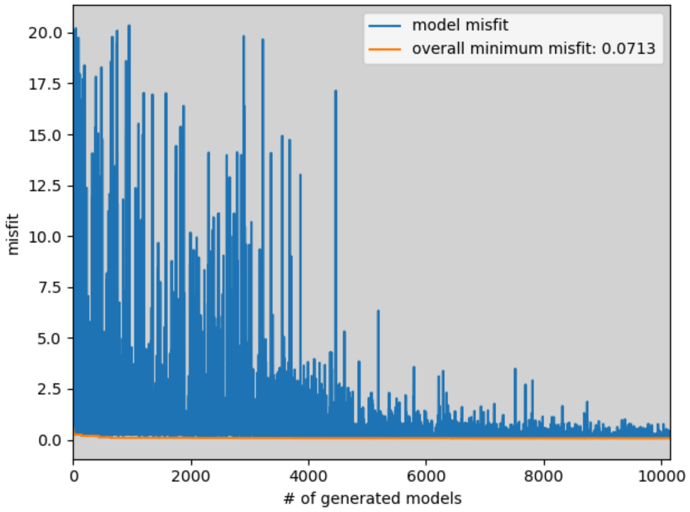

Figure E.1.: Misfit evolution of joint inversion with $f_0 = 1.19$ Hz

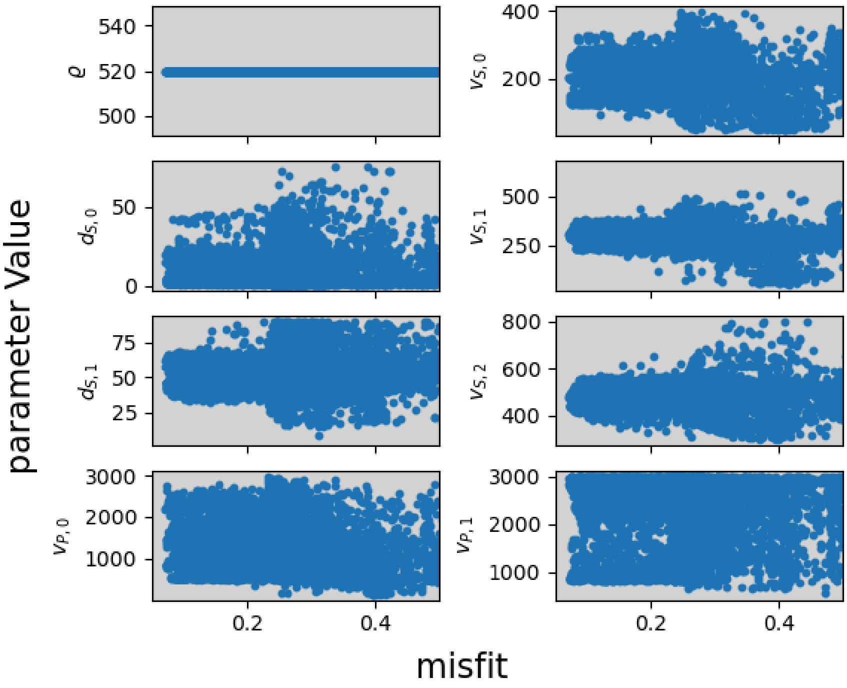

Figure E.2.: Parameter space of joint inversion with $f_0 = 1.19$ Hz

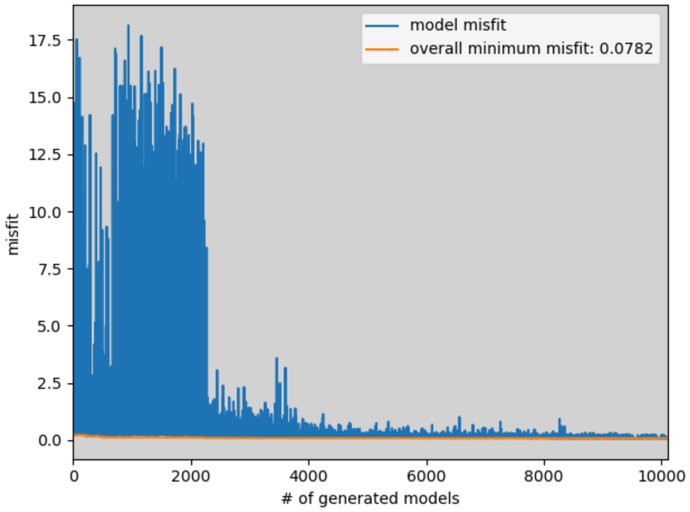

Figure E.3.: Misfit evolution of joint inversion with $f_0 = 0.91$ Hz

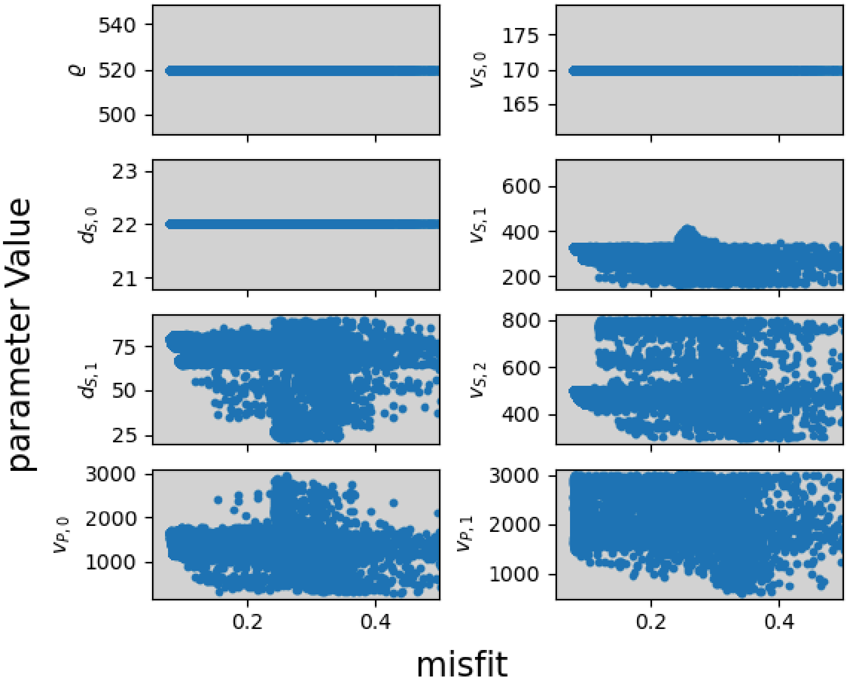

Figure E.4.: Parameter space of joint inversion with $f_0 = 0.91$ Hz

F. Results of magnetic survey by Napoli et al. (2021)

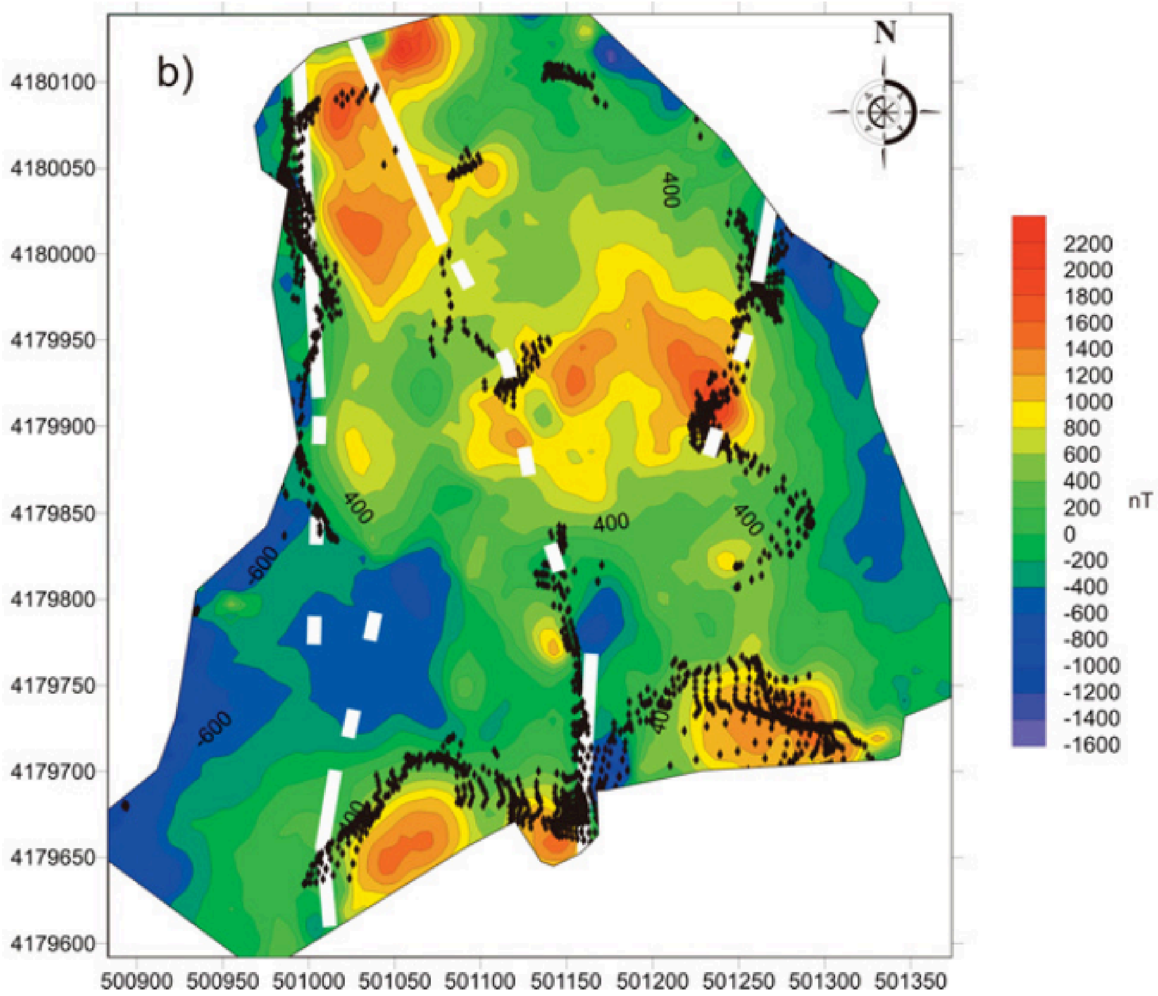

Figure F.1.: One solution for the magnetic anomly causing geological bodies on PDC (from: Napoli et al., 2021)

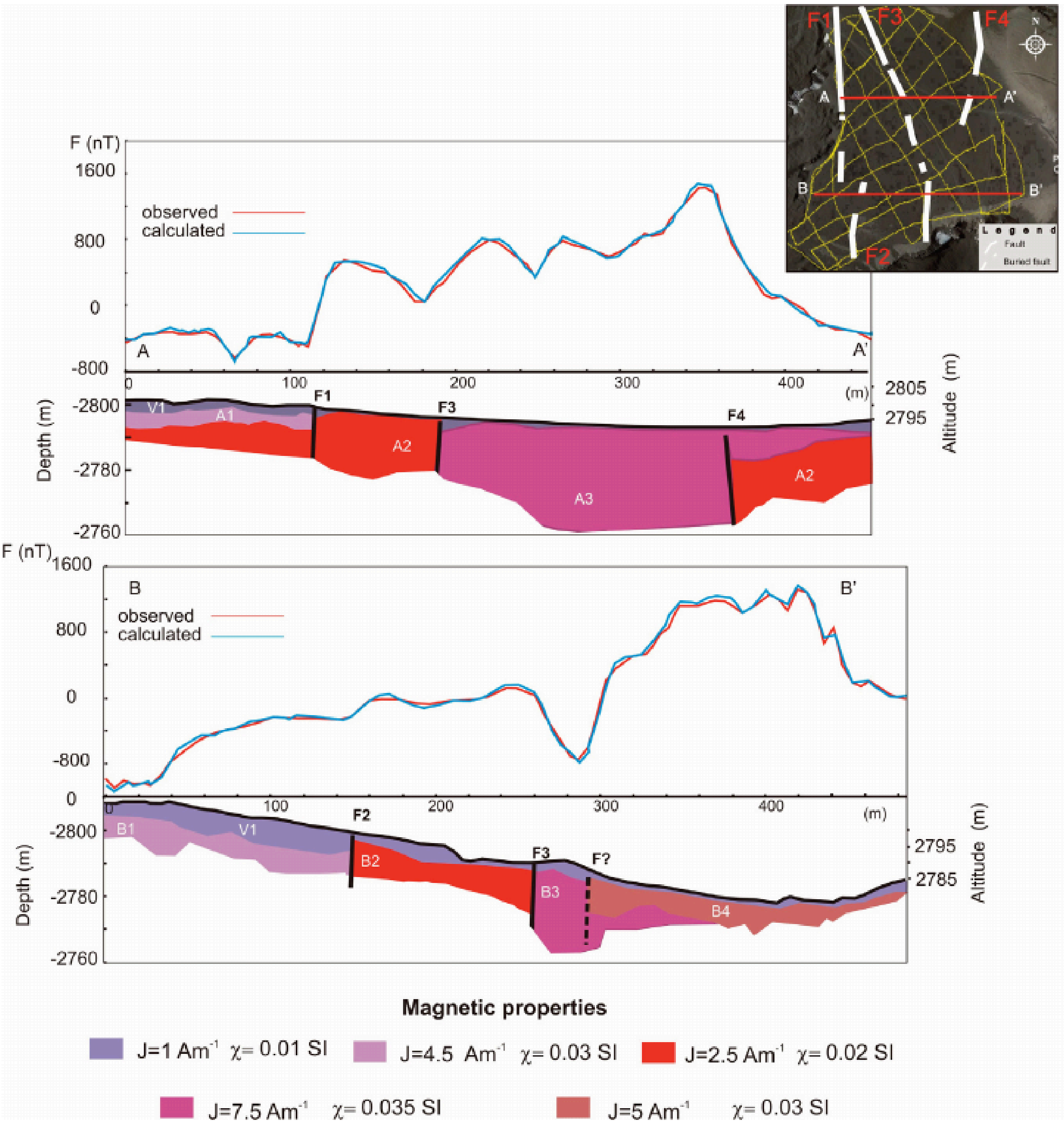

Figure F.2.: Modelled profiles of magnetic properties on PDC, location of profiles are given in inset (from: Napoli et al., 2021)